



**HAL**  
open science

## Unconventional coke composition during high temperature anisole disproportionation on zeolites

Nathan Pichot, Nourrdine Chaouati, T. Lemaitre, Mohammad Fahda, Valentin Valtchev, Svetlana Mintova, Jean-Pierre Gilson, Anthony Dufour, Ludovic Pinard

### ► To cite this version:

Nathan Pichot, Nourrdine Chaouati, T. Lemaitre, Mohammad Fahda, Valentin Valtchev, et al.. Unconventional coke composition during high temperature anisole disproportionation on zeolites. *Applied Catalysis A : General*, 2024, 682, pp.119808. 10.1016/j.apcata.2024.119808 . hal-04628985

**HAL Id: hal-04628985**

**<https://hal.science/hal-04628985>**

Submitted on 28 Jun 2024

**HAL** is a multi-disciplinary open access archive for the deposit and dissemination of scientific research documents, whether they are published or not. The documents may come from teaching and research institutions in France or abroad, or from public or private research centers.

L'archive ouverte pluridisciplinaire **HAL**, est destinée au dépôt et à la diffusion de documents scientifiques de niveau recherche, publiés ou non, émanant des établissements d'enseignement et de recherche français ou étrangers, des laboratoires publics ou privés.

# Unconventional coke composition during high temperature anisole disproportionation on zeolites

N. Pichot<sup>a,b,c</sup>, N. Chaouati<sup>c</sup>, T. Lemaitre<sup>c</sup>, M. Fahda<sup>c</sup>, V. Valtchev<sup>c</sup>, S. Mintova<sup>c</sup>, J-P. Gilson<sup>c</sup>, A. Dufour<sup>b</sup>, L. Pinard<sup>c</sup>.

<sup>a</sup> Institut de Chimie des Milieux et Matériaux de Poitiers, IC2MP, UMR 7285, Poitiers, France

<sup>b</sup> Laboratoire Réactions et Génie des Procédés, LRGP, UMR 7274, Université de Lorraine, France.

<sup>c</sup> Laboratoire de Catalyse et Spectrochimie, LCS, UMR 6506, ENSICAen, France.

Corresponding author: [ludovic.pinard@ensicaen.fr](mailto:ludovic.pinard@ensicaen.fr)

## Abstract

Catalyst deactivation and shape selectivity in evolved products and retained coke are studied on medium, large and extra-large pore zeolites with varying Si/Al ratios in the disproportionation of anisole. Deactivation modelling as a function of time on stream highlights the key role of the catalyst **pore** volume. Changes in selectivity between the primary (methylanisole) and secondary (cresol) products are due to the overtaking of one path over a second for the production of cresol. The nature of the products (methyl phenols) inhibits the formation of “usual” polyaromatic and non-oxygenated coke via the Sullivan mechanism, leaving only adsorbed oxygenated monoaromatics, available for transalkylation reactions with the feed, having adsorbed and fouled most of the available surface in the catalyst channels.

Keywords: Anisole, Zeolite, Zeolite pore size, coke, phenolic compounds.

## Introduction

Catalytic Fast Pyrolysis (CFP) on zeolites is a promising route to produce high value hydrocarbons from biomass-derived feedstocks [1–4] as it avoids a costly hydrodeoxygenation (highly exothermic reaction at high pressure with H<sub>2</sub> consumption) [5,6]. However, during CFP a fast catalyst deactivation occurs due to coke formation [7,8]. Overcoming this obstacle is a necessary step to scale-up and commercialise the process [9]. To better understand the fundamentals of such deactivation, focusing on the conversion of single model molecules is a first step to apprehend the behaviour of the oxygenated hydrocarbons present in pyrolytic bio-oils.

Consequently, two options are available: co-feeding these model molecules with well-known feeds, or pure model molecules (hydroxy-, methoxy-functions, aldehydes, ketones, furans...). Among these options, co-feeding phenol with a classical FCC charge has been explored extensively by Graça et al. [10–15]. Phenolics conversion has also been studied in depth by Gayubo et al. [16,17] and Adjaye et

coll. [18]. Model molecules such as furans, guaiacol and other phenolics, and anisole conversion under CFP operating conditions have already been reported [7,19–26]. Among these model compounds, anisole is a good proxy for the methoxy-substituted aromatics in biomass pyrolysis (present in bio-oils derived from lignin pyrolysis), as it consists of a C<sub>6</sub> aromatic ring and a CH<sub>3</sub>O-group.

Anisole transformation on acidic zeolites is a bimolecular reaction (disproportionation) and produces mainly methylated phenolics, and very few non-oxygenated compounds [20–22,27]. Previous work showed a fast deactivation due to the formation and subsequent strong adsorption of phenolics, the primary reaction products [20,22]. The main reaction mechanism is a series of transalkylations producing the so-called “coke” retained on the catalyst surface and/or porosity [22], and causing its deactivation [28–34].

The formation and nature of deactivating species, are usually highly dependent on temperature:

- i) Low temperatures (up until around 723 K) [35,36] lead to the formation, by condensation and rearrangement, of alkenes (aliphatic or cyclical), dienes, naphtho-aromatics, strongly adsorbed on the active sites;
- ii) Higher temperatures (from around 723 K) [35,36] yield polyaromatic hydrocarbons (PAH), such as pyrene, indene..., by hydrogen transfers and dehydrogenating coupling [36]. Steric hindrance on these heavy polyaromatics traps them in the zeolite microporosity [36].

High temperature coke formation is a highly shape-selective and complex process [36,37]. Zeolite structure determines the size and shape of the molecules retained in the channels (methylpyrenes are formed on **MFI**, coronene-like coke forms on **FAU**, and the monodimensional channels of **MOR** produce linear molecules, such as phenanthrenes and anthracenes [28,36,38]). One of the most common mechanism includes constant alkylation of aromatic cycles, with paring reactions leading to autocyclisation of the precursors (**Scheme S1 in supplementary material**) [39–41]. Another path necessitates low reactant partial pressure, and consists in dehydrogenating coupling of adsorbed coke precursors [38]. Deactivating species can result from condensation of the actives species produced by hydrocarbon pool cycle (alkylbenzene) retained on the micropores [42]. This condensation on confined zeolites micropores is faster at lower contact time [43] and low olefin pressure [38]. In the case of small pore opening zeotype like SAPO-34, continue alkylation and cyclization of cycloalkanes or aromatics with olefins is supposed to be the main cause of formation of reticulate structure composed of carbon-chain bridged cycloalkanes and aromatics[44].

As of oxygenated aromatic molecules resulting from biomass pyrolysis processing on acidic zeolites, far less details are available on the “coke” composition and effect of porosity on its formation than on conventional PAH coke. Co-feeding phenol with oil-derived FCC feedstocks showed that phenol was strongly adsorbed on Brønsted acid sites in the zeolite porosity: Graça et al. reported that phenol affected the coke formation rate and quantity, and identified mostly polyaromatics and adsorbed phenol in the coke [10,11]. Zhang et al. studied furan CFP on **MFI** and reported no oxygenates in the coke although no component identification was performed [7]. Ma et al. studied Lignin CFP on multiple catalysts (**FAU**, **MFI**, **\*BEA** and amorphous silica-alumina), but reported only the amount of coke produced [45]. Other studies focusing on the minimization of coke formation do not discuss coke composition [46]. Liu et al. found some oxygenates (methylated cyclopentenones) in the coke on methanol to hydrocarbon spent zeolite catalysts, identified as coke precursors in the formation of conventional polyaromatic coke [47].

In the case of anisole disproportionation on zeolites, the usual PAH were not found in MFI, and instead, deactivation was due to monoaromatic phenolic products strongly adsorbed on active sites in the zeolite channels [22], indicative of low-temperature coke [22,36]. Previous work showed a strong impact of Si/Al ratio on the catalytic activity [48], and of catalyst structure [21]. They could impact deactivation and coke formation mechanism and make-up, given the aforementioned coke shape selectivity effects at high temperatures.

This contribution studies anisole disproportionation with 10 (**MFI**) and 12 membered-ring (MR) (**\*BEA**, **MOR**, **FAU**) zeolites as well as a newly discovered 16 MR (**JZO**) zeolite; the latter possesses a 3D channel network, and supercages [49,50]. We will first focus on the effects of structure and acidity on catalytic activity, product yield, and isomer selectivity. Second, we study the coke deposits and the effect of zeolite structure and acidity on its composition, formation mechanism, finally its effect on the zeolite deactivation mode.

Does anisole disproportionation produce the same coke species previously reported for **MFI** with the other structures ? Is it, yet again, a shape-selective process, with larger pores allowing for the growth of polyaromatic hydrocarbons?

## Experimental section

**Catalysts:** One **MFI** (ZSM-5) zeolite is provided by Tosoh (Si/Al = 12), HSZ-820NHA). Another **MFI**, as well as the three **FAU** and one **\*BEA** (beta zeolite) are sourced from Zeolyst (respectively **MFI** Si/Al = 43 – CBV8014 –, **FAU** (Y) Si/Al = 6, 15, 30 – CBV712, CBV720, CBV730 –, and **\*BEA** Si/Al = 12.5 – CP814e). The second beta zeolite is supplied by UOP (**\*BEA** Si/Al = 13.7 – Sample ID 75085-2042003829). One **MOR** zeolite is provided by ZEOCAT (**MOR** Si/Al = 10 – ZM-510-Z3464). Another mordenite catalyst with higher Si/Al ratio is also used (**MOR** Si/Al = 80). Finally, the **JZO** zeolite is synthesised with the method described by **Fahda et al.** (**JZO** Si/Al = 23.4 – ZEO-1)[50]. **MFI**, **\*BEA** and **MOR** zeolites are in  $\text{NH}_4^+$  form, therefore calcination is performed to convert to the protonic form: under  $\text{N}_2$  ( $P_{\text{atm}}$ , 100 mL.min<sup>-1</sup>) at 373 K for an hour (5 K.min<sup>-1</sup> from room temperature) for drying, then under air ( $P_{\text{atm}}$ , 100 mL.min<sup>-1</sup>) at 823 K for 6 hours (10 K.min<sup>-1</sup>).

Catalysts are named with their structure followed by their Si/Al ratio in parentheses. Example: **MFI**(43).

**Characterizations:** The Si/Al ratio is measured by ICP-OES. Samples are dissolved in an acid solution (4 mL  $\text{HNO}_3$  >68%, 3 mL  $\text{HCl}$  34-37%, 1 mL  $\text{HF}$  47-51% and 42 mL Ultra-pure water), with microwave assistance (Anton-Paar Multiwave Pro), and analysed with ICP-OES – 5110 Agilent VDV.

Pyridine adsorption (423 K) monitored by infrared (IR) spectroscopy (*Nicolet Magna FTIR iS50* spectrometer) is used to quantify acidity (Pyr-FTIR) [51,52]. Samples are shaped into wafers and activated *in-situ* in the IR cell (under air, ambient to 623 K for 15 h for fresh catalysts, and **under vacuum at** 423 K for spent samples). The interaction between pyridine and the acid sites of zeolites produces some characteristic bands for pyridine adsorbed on Brønsted and Lewis acid sites in the 1300-1700  $\text{cm}^{-1}$  region: pyridinium ions (1490, 1545, 1640  $\text{cm}^{-1}$ ) and coordinated pyridine (1455, 1490, 1600-1630  $\text{cm}^{-1}$ ). Their concentration is calculated using the Beer-Lambert-Bouguer's law:

$$C = \frac{A}{\epsilon} * \frac{S}{m} * 1000 \quad (\text{Eq. 1})$$

where C is the acid sites concentration ( $\mu\text{mol.g}^{-1}$ ), A the band's area (absorption.cm<sup>-1</sup>), S the wafer's surface (2 cm<sup>2</sup>), m the mass of the wafer (mg), and  $\epsilon$  the molar extinction coefficient (cm.μmol<sup>-1</sup>).

Molar extinction coefficients were previously determined to be respectively  $1.13 \text{ cm}\cdot\mu\text{mol}^{-1}$  and  $1.28 \text{ cm}\cdot\mu\text{mol}^{-1}$  for Brønsted and Lewis acid sites [52].

Nitrogen sorption measurements are carried out at 77 K, from 0 till 100 kPa (absolute pressure) with a *Micromeritics 3Flex* apparatus. Fresh samples are degassed for 15h at 623 K. For spent samples, degassing is performed at ambient temperature (preventing oxidation and/or thermal desorption). The microporous volume ( $V_{\text{micro}}$ ) and the external surface area are calculated from the t-plot curve using the Harkins-Jura method and a thickness range between 4.5 and 5.8 Å. Total porous volume ( $V_{\text{pore}}$ ) is calculated with a single point adsorption method at around  $P/P_0 = 0.988$ , and the specific surface area is calculated with the BET method.

Crystal sizes are assessed with SEM imagery (values from previous works [50,53]).

The coke mass content in the catalyst channels is assessed by thermogravimetric analysis (TGA). Approximately 20 mg of the spent catalyst are placed in a platinum crucible and in a SDT Q600 TD/TG unit. The sample analyses are carried out under air flow ( $100 \text{ mL}\cdot\text{min}^{-1}$ ) between 303 K (plateau for 10 min) and 1173 K ( $10 \text{ K}\cdot\text{min}^{-1}$ ). The final temperature is maintained for 10 min, then allowed to cool down.

Coke extraction on spent catalysts allows for its molecular identification and quantification [29]. It proceeds by complete dissolution of the zeolite framework in an HF solution (aqueous hydrofluoric acid, 40%) and the freeing the hydrocarbon deposits. Boric acid ( $\text{H}_3\text{BO}_3$ ) captures the excess fluor ions, and sodium bicarbonate neutralises both acids in the resulting mixture. Hydrocarbons are recovered by liquid-liquid extraction with  $\text{CH}_2\text{Cl}_2$ . Should some insoluble hydrocarbons (*e.g.* heavy polyaromatics) remain in suspension, they are usually recovered by a Büchner filtration [41], but none are found here.

The organic liquid phase is then injected in a GC-MS (GC-MS 8700SQ, Scion, *Scion5-MS column*) and GC-FID (Bruker 456-GC, *Scion5-MS column*) for identification and quantification.

A blank test for the coke extraction conditions is carried out. Anisole, phenol and o-cresol are injected in GC-MS alone and after having undergone the coke extraction process described above. Then, a mixture of anisole and phenol is injected, alone and after the extraction process. Cresol is a product of the reaction of anisole and phenol in the reaction conditions [22]. If HF triggered the transalkylation reaction described in previous work, or any other, between anisole and phenol, the chromatograms in **Figure S1** would show it. No reaction is found to take place: no fluorination, hydrolysis, etc. took place during the test, and thus the dissolution of the zeolite framework and coke molecules adsorbed therein in HF does not affect the nature of the coke species during extraction.

**Catalytic tests:** Catalytic tests take place in a continuous down-flow tubular fixed bed reactor. Before test, catalysts are sieved to particles of  $0.2 < \phi < 0.4 \text{ mm}$  diameter (pellets formed under 500 kg then crushed in a mortar). Catalyst pre-treatment is as follows: heating to 373 K ( $1 \text{ K}\cdot\text{min}^{-1}$  from ambient), with a 1 h plateau, to avoid any steaming damage from adsorbed water. Further heating ( $1 \text{ K}\cdot\text{min}^{-1}$ ) to 673 K followed with a 1 h plateau at the final temperature. Liquid anisole is then injected ( $0.01 \text{ mL}\cdot\text{min}^{-1}$ ) with a *Metrohm 725 Dosimat* and vaporized at the reactor inlet. The operating conditions are:  $P_{\text{anisole}} = 0.048 \text{ atm}$ ,  $\text{N}_2$  flowrate (STP) =  $100 \text{ mL}\cdot\text{min}^{-1}$ ,  $T = 673 \text{ K}$ ,  $0.02 < W/F^\circ < 0.17 \text{ g}_{\text{cata}}\cdot\text{h}\cdot\text{g}_{\text{feed}}^{-1}$ . All lines after the reactor are heated at 623 K to avoid condensation of reactant and products ( $T_{\text{lines}} > T_{\text{boil}} + 50$ ).

Reaction products were quantified online with a GC-FID (Bruker 456-GC, *Scion5-MS column*, 30 m - 0.25 mm - 25  $\mu\text{m}$ ). The setup includes ten 500  $\mu\text{L}$  sample loops (heated at 493 K), to store the

reaction products at different (programmable) times-on-stream before injection, for a kinetic study of the catalyst deactivation. Blank tests (empty reactor) were performed, to rule out any participation of thermal reaction of anisole and none is found at 673 K.

Conversion ( $X_t$ , %), mass yields ( $Y_{i,t}$ , wt.%) and selectivities ( $S_{i,t}$ , %) were calculated as follows:

$$X_t(\%) = \left(1 - \frac{A_{Anisole,t}}{A_{total,t}}\right) * 100 \quad (\text{Eq. 2})$$

$$Y_{i,t}(\text{wt. \%}) = \left(\frac{A_{i,t}}{A_{total,t}}\right) * 100 \quad (\text{Eq. 3})$$

$$S_{i,t}(\%) = \left(\frac{Y_{i,t}}{X_t}\right) * 100 \quad (\text{Eq. 4})$$

Where  $A_{Anisole,t}$ ,  $A_{total,t}$  and  $A_{i,t}$  represent the areas of the anisole, the sum of all the peaks and the peak of the product  $i$ , at any given  $t$  time, respectively.

**Eq. 2** does not take into account the feed that is converted into coke, because the quantities are so small they can be neglected (around 7.5 mg at most, versus around 6 g of feed after 1h reaction time).

## Results and discussion

### 1. Zeolites Characterisation

The aim of the present work is to assess the effects of different zeolite structures and acidity on anisole disproportionation (catalyst activity and deactivation, main product selectivities, coke formation). Thus, five structures were chosen: **MFI** (10 MR, interconnected straight and sinusoidal channels) [54], **\*BEA** (12 MR, 3D interconnected straight channels) [55], **MOR** (12 and 8 MR, 2D straight channels, side pockets) [56], **FAU** (12 MR, 3D, supercages) [57] and **JZO** (16 and 12 MR, 3D interconnected straight channels, supercages) [58]. At least two Si/Al ratios (i.e. BAS concentrations) were selected for each commercial catalyst, in order to distinguish the structural effects from those originating from acidity. The pore volumes (micro- and meso-pores), external surface and BET specific areas, are presented in **Table 1**.

Micropore volumes are as expected: **MFI**:  $\approx 0.17 \text{ cm}^3 \cdot \text{g}^{-1}$ , **\*BEA**:  $\approx 0.22 \text{ cm}^3 \cdot \text{g}^{-1}$ , **MOR**:  $\approx 0.20 \text{ cm}^3 \cdot \text{g}^{-1}$ , **FAU**:  $\approx 0.30 \text{ cm}^3 \cdot \text{g}^{-1}$  [52]. In Beta zeolites (\*BEA), the mesopores result from the agglomeration of nanometre-sized crystals [59,60], whereas in Y zeolites, the mesopores are intracrystalline and were generated during steaming post-treatment. The high external surface area of beta zeolites is consistent with their small crystal size.

**Table 1:** Structural, chemical and textural properties of the commercial and synthesized zeolites

Structure	Pore network (Å)	Si/Al <sup>a</sup>	[PyH <sup>+</sup> ] <sup>b</sup> (μmol.g <sup>-1</sup> )	[PyL] <sup>b</sup> (μmol.g <sup>-1</sup> )	V <sub>micro</sub> <sup>c</sup> (cm <sup>3</sup> .g <sup>-1</sup> )	V <sub>meso</sub> <sup>c</sup> (cm <sup>3</sup> .g <sup>-1</sup> )	External Surface <sup>c</sup> (m <sup>2</sup> .g <sup>-1</sup> )	BET Surface <sup>d</sup> (m <sup>2</sup> .g <sup>-1</sup> )	Crystal size (nm)
<b>MFI</b>	{[100] <b>10</b> 5.1 x 5.5 ↔	12	641	183	0.16	0.08		415	
	[010] <b>10</b> 5.3 x 5.6}***	43	281	42	0.16	0.05	82	452	500 <sup>e</sup>
<b>*BEA</b>	<b>12</b> 6.6 x 6.7* ↔	12.5	487	352	0.22	0.58	201	535	30 <sup>f</sup>
	<b>12</b> 5.6 x 5.6*	13.7	641	93	0.22	0.27	192	496	50
<b>MOR</b>	[001] <b>12</b> 6.5 x 7.0* ↔	10	360	281	0.20	0.05	50	445	
	[001] <b>8</b> 2.6 x 5.7**	80	97	37	0.20	0.10	102	485	
<b>FAU</b>		6	481	186	0.27	0.15	147	722	
	[111] <b>12</b> 7.4 x 7.4***	15	270	101	0.31	0.21	155	873	370 <sup>f</sup>
		30	88	18	0.34	0.20	166	742	
<b>JZO</b>	[100] <b>16</b> 10.6 x 9.4 / 10.5 x 9.6 *** ↔ [100] <b>12</b> 6.6 x 6.8	23.4	513	155	0.29	0.10	160	861	470 <sup>f</sup>

<sup>a</sup> Calculated from the mass ratios measured by ICP-OES. <sup>b</sup> Pyridine adsorption-desorption (423 K) monitored by FTIR. <sup>c</sup> N<sub>2</sub>-physisorption at 77 K, calculated with the t-plot curve of the Harkins-Jura method. <sup>d</sup> N<sub>2</sub>-Physisorption at 77 K, BET method. SEM values given by previous works on the catalysts <sup>e</sup> [53], <sup>f</sup> [50]

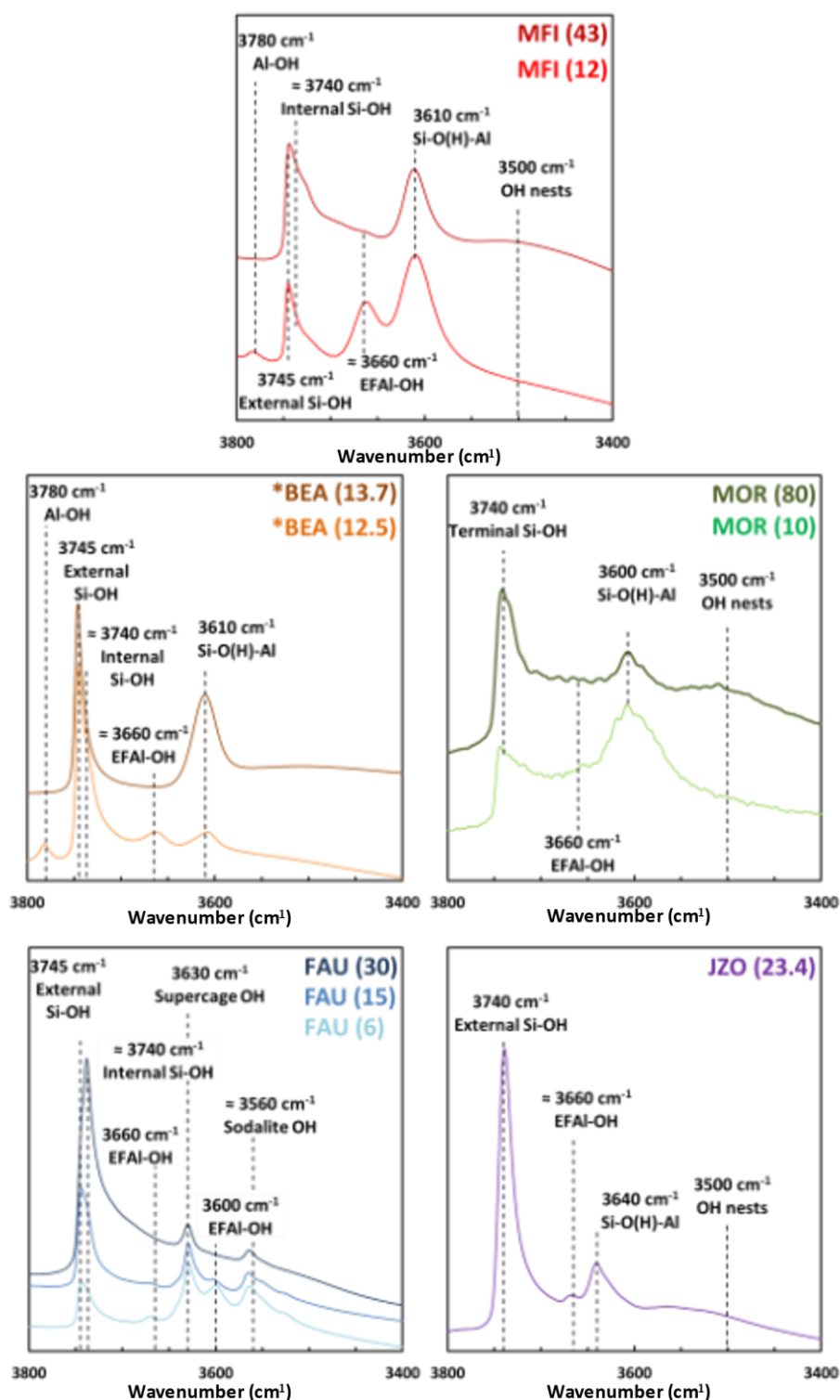


**Figure 1** FTIR spectra of the hydroxyl region ( $3800 - 3400 \text{ cm}^{-1}$ ) of the fresh catalysts. Intensities (a.u.) are normalised to 20 mg samples for each structure.

**Figure 1** shows the OH stretching vibration region of the different zeolite catalysts. Each exhibit their respective characteristic bands:

**MFI**, **\*BEA**, and **MOR** display peaks indicative of bridged hydroxyls (Si-O(H)-Al), between  $3600$  and  $3610 \text{ cm}^{-1}$ , and **JZO** at  $3640 \text{ cm}^{-1}$ [50,61]. These bridged hydroxyls correspond to the Brønsted acid sites. Faujasites show unique bands around  $3630$  and  $3560 \text{ cm}^{-1}$ , corresponding respectively to



bridged hydroxyls in supercages and sodalite cages. On **\*BEA** (12.5) and **MFI** (12), a small band at  $3780\text{ cm}^{-1}$ , belongs to Al-bonded OH groups [61].

The vibrational band between  $3740\text{--}3745\text{ cm}^{-1}$  is attributed for non-acidic terminal (isolated) silanol species that is common for all zeolitic materials and can be observed for all the zeolites characterized in Figure 1. Additionally, a low intensity broad vibrational band between  $3400\text{--}3500\text{ cm}^{-1}$  can be observed is observed for **MFI** (43), **BEA** (13.7), **MOR** (80) and **JZO** which is known to result from the so called silanols nests which are internal silanol species engaged in hydrogen bonding among each other [61]. However, for JZO we have shown previously that this broad vibrational band also contains a population of Bronsted acid sites [50].

**MFI** (12), **\*BEA** (12.5), **MOR** (10), **FAU** (6) and **JZO** (23.4) display a broad band around  $3660\text{ cm}^{-1}$  indicative of extra-framework-Al-bonded hydroxyl groups (EFAl-OH) [61,62]. **FAU** (6) and **FAU** (15), albeit to a lower extent, exhibit a small band at  $3600\text{ cm}^{-1}$  (EFAl-OH) [61].

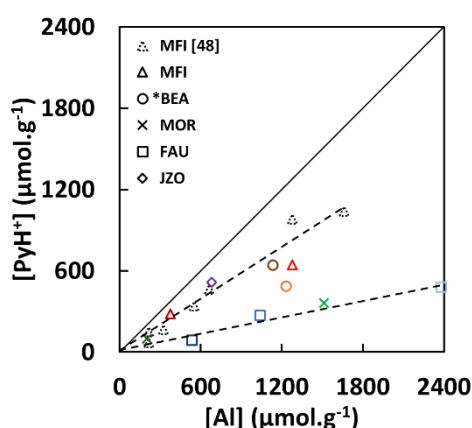


**Figure 2:** Evolution of Bronsted acid site concentration (BAS) with Al content ( $\mu\text{mol.g}^{-1}$ ) of the various zeolites. Black full line:  $[\text{PyH}^+] = [\text{Al}]$ .

**MFI:** dotted symbols are from previous work [48].

**Figure 2** shows the Brønsted acid sites (BAS) concentrations of the various zeolites probed by Py-FTIR as a function of their aluminium content. BAS concentrations range from 88 to  $641\text{ }\mu\text{mol.g}^{-1}$  (**Table 1**). They are proportional to aluminium content, and this suggests that most aluminium atoms are in the framework. **\*BEA** (12.5), having EFAl-OH (**Figure 1**), has a lower BAS concentration, despite a higher aluminium content than **\*BEA** (13.7) [63]. The values of  $[\text{PyH}^+]$  of the **FAU** are relatively low due to the presence of BAS in sodalite cages, less accessible to pyridine. Acidity could be underestimated slightly for these catalysts [61].

## 2. Anisole disproportionation

Anisole disproportionation at 673 K under  $\text{N}_2$  flow ( $0.048\text{ atm}$  partial pressure of anisole) is performed on each catalyst at different contact times ( $0.02\text{ g}_{\text{cata}}\cdot\text{h}\cdot\text{g}_{\text{anisole}}^{-1} < W/F^\circ < 0.17\text{ g}_{\text{cata}}\cdot\text{h}\cdot\text{g}_{\text{anisole}}^{-1}$ ).

### 2.1. Effects of structure, BAS concentration on TOF and deactivation modelling

**Figure 3a** and **3b** show the initial Turnover Frequencies ( $\text{TOF}_0$ ) evolution of the catalysts, as a function of their initial Brønsted acidities. Initial TOF are used, in order to compare the catalysts in their initial, pristine state.  $\text{TOF}_0$  is calculated as follows:

$$\text{TOF}_0 = \frac{\alpha_0}{[\text{PyH}^+]_0} \quad (\text{Eq. 5})$$

With  $\alpha_0$  the initial activity obtained from the slope of the line drawn with  $|\ln(1-X_0)| = f(W/F)$  for low conversions (**Figure S3**).

In **MFI**, the highest  $TOF_0$  are three times lower than in **FAU** and **\*BEA**, while the curves retain the same shape. This indicates that the larger pores **FAU** and **\*BEA** promote the bimolecular reactions involved in anisole conversion.

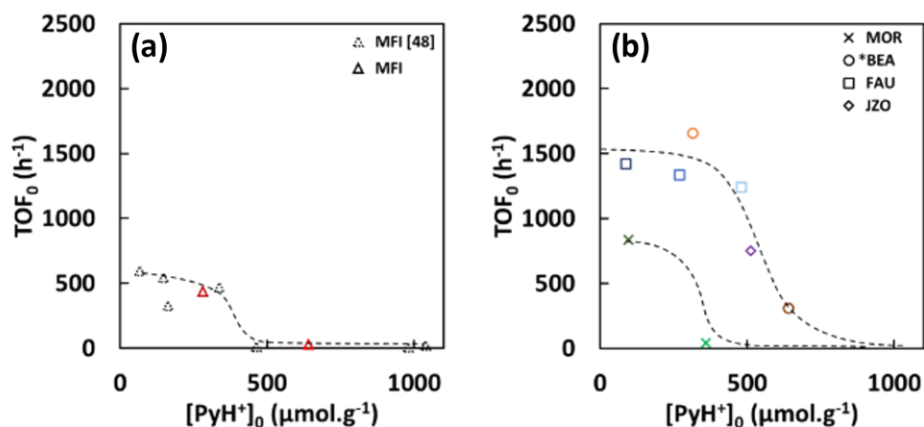


**Figure 3:**  $TOF_0$  evolution as a function of their BAS concentration (a) **MFI** and (b) the 12 and 16 MR catalyst.

**MFI:** dotted symbols are results from previous work [48].

All dotted lines are only to guide the eye.

The drop in  $TOF_0$ , previously reported for **MFI**, also occurs with the 12 and 16 MR catalysts. Higher acidity **MFI**, with very low activity, have negligible  $TOF_0$ . The larger pores of **FAU**, **\*BEA** and **JZO** mitigate the drop, and the interconnectivity of the channels plays a role as well: the three-dimensional **FAU**, **\*BEA** and **JZO** provide higher  $TOF_0$ , even at higher acidities, while the two-dimensional **MOR** behaves more like an **MFI**.

**Figure 4** shows the catalyst deactivation over 1h of reaction. Independently of the zeolite structure and acidity, deactivation is fast and important and levels after 0.3 h.

**\*BEA** and **MOR** catalysts behave as **MFI** (43), the highest acidity leading to the lowest residual activity; **MOR** (10) is almost inactive irrespective of TOS.

In the case of the **FAU** catalysts, a higher acidity promotes a higher initial activity, but also faster deactivation rates and lower final activities: **FAU** (6) has a final activity 30 times lower than at the start of the run, 6 times for **FAU** (15) and 7 times for **FAU** (30).

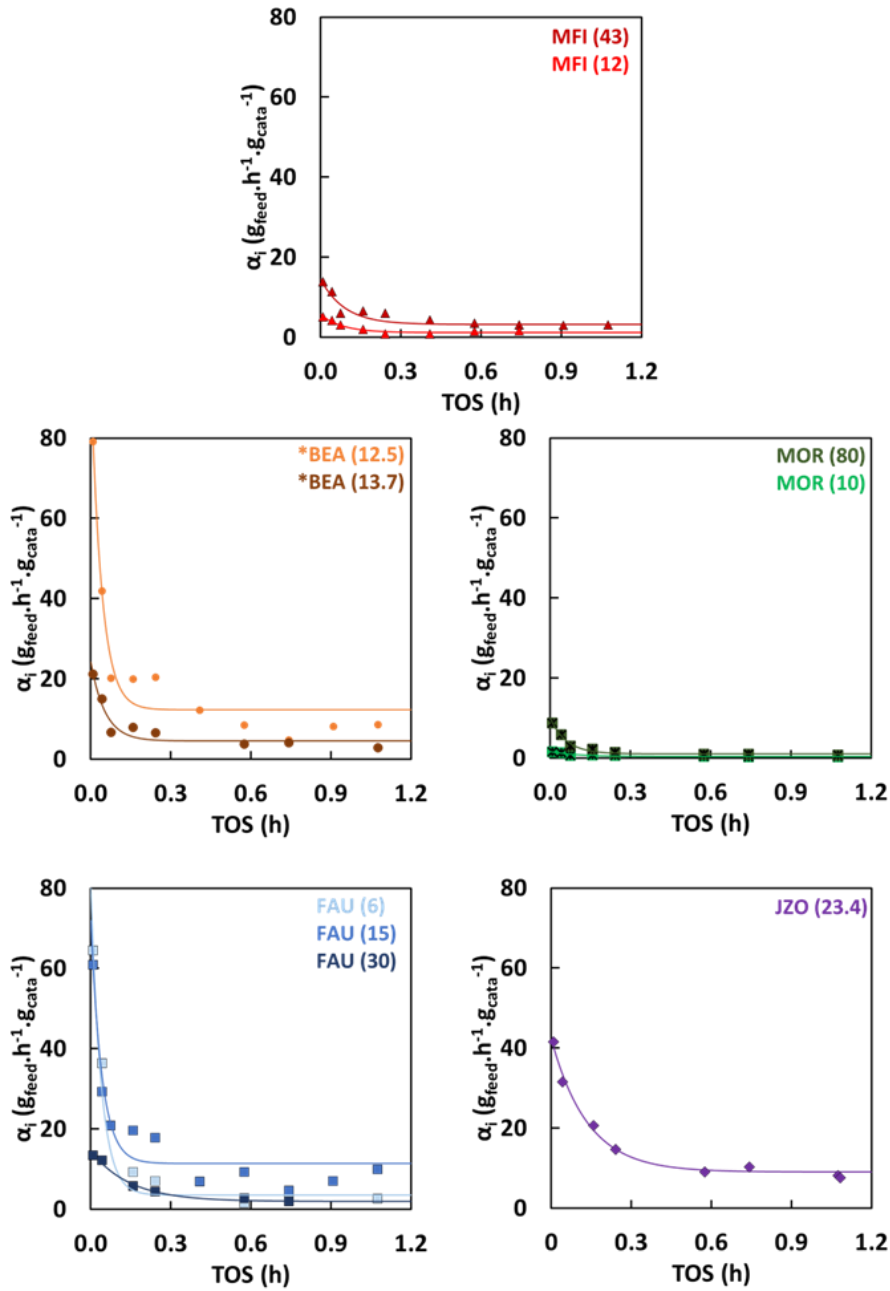


**Figure 4:** Evolution of activity with time on stream for anisole disproportionation on zeolites.

It was shown in previous work that three out of the four most stable tetrahedral sites for aluminium substitution (hence BAS) are most likely located within the 12 MR pores of JZO (23.4), thus its activity is reminiscent of \*BEA and FAU. It deactivates in the same way as the others, but its final activity remains as high as those of \*BEA (12.5) and FAU (15). A possible explanation for this is the low BAS density in the 16 MR channels, which could help with the outward diffusion of the reaction products, allowing for slower deactivation of the catalyst [50].

All activity curves follow an inverse exponential law, which is drawn on Figure 4 and was determined by computational fitting of the data points :

$$\alpha_i = \alpha_1 * e^{-k_D * TOS} + \alpha_2 \quad (\text{Eq. 6})$$

$\alpha_0$  (i.e.  $\alpha_1 + \alpha_2$ ) is the initial catalyst activity, and  $k_D$  is the deactivation constant for each catalyst.

**Table 2** shows these values for each catalyst, as well as coke content and coefficient of determination, the latter showing its applicability to all our zeolite catalysts.

The higher  $k_D$ , the faster and higher the catalyst deactivation. It is highest for **FAU** (6), **FAU** (15), and **\*BEA** (12.5).  $\alpha_1$  represents the active species that will cease participating to the reaction, while  $\alpha_2$  represents the active species responsible for the (low) residual, steady-state activity.

**Eq. 6** is reminiscent of the deactivation function previously used by Guisnet and Ribeiro [36]:

$$\phi_i = \frac{\alpha_i}{\alpha_0} = \frac{\alpha_1}{\alpha_0} e^{-k_D * TOS} + \frac{\alpha_2}{\alpha_0} \quad (\text{Eq. 7})$$

Where the dimensionless number  $\phi_i$  is the deactivation of the catalyst at any TOS (h) and the added factors ( $\frac{\alpha_1}{\alpha_0}, \frac{\alpha_2}{\alpha_0}$ ) indicate that deactivation is not solely a factor of coke deposition.

**Table 2:** activities ( $\alpha$ ), deactivation constants ( $k_D$ ), determination coefficient ( $R^2$ ) and coke content for each catalyst. Grey row: **MFI** reference from [22].

Structure	Si/Al	$\alpha_i = \alpha_1 * e^{-k_D * TOS} + \alpha_2$				Coke content (wt.%)
		$\alpha_1$ ( $g_{\text{feed}} \cdot h^{-1} \cdot g_{\text{cata}}^{-1}$ )	$\alpha_2$	$k_D$ ( $h^{-1}$ )	$R^2$	
<b>MFI</b>	12	4.5	1.2	12.2	0.92	7.3
	43	11.2	3.2	11.1	0.96	7.6
<b>*BEA</b>	12.5	83.3	12.4	24.9	0.95	11.2
	13.7	19.7	4.6	18.6	0.92	14.9
<b>MOR</b>	10	1.2	0.4	9.6	0.89	1.9
	80	8.8	1.1	16.6	0.99	3.4
<b>FAU</b>	6	77.4	3.6	26.2	0.95	11.1
	15	60.5	11.4	24.2	0.93	10.3
	30	12.6	2.0	6.8	0.99	6.7
<b>JZO</b>	23.4	33.2	9.1	7.3	0.99	11.2

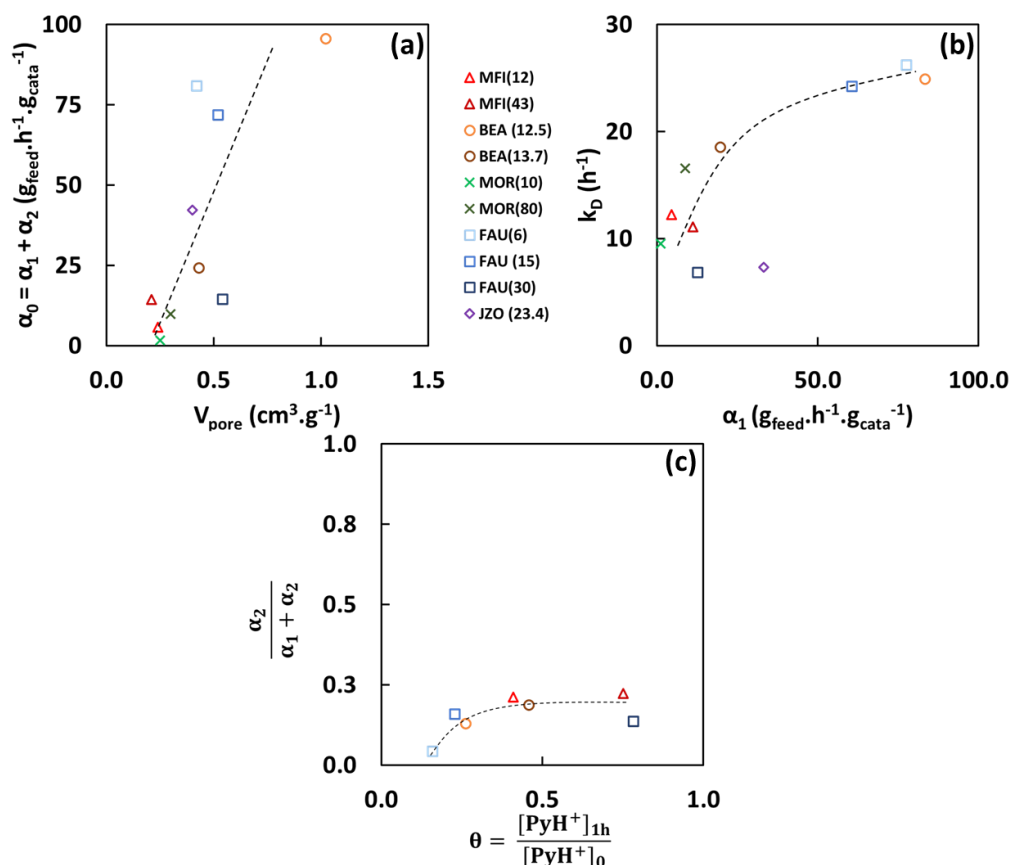


**Figure 5:** Dependence of the deactivation law on the textural and physico-chemical properties of the catalyst: **(a)** initial activity vs. porous volume; **(b)** deactivation constant vs. pre-exponential factor ( $\alpha_1$ ); **(c)** residual activity contribution vs. remaining fractional Brønsted acidity after 1h.

$$\theta = \left( \frac{[\text{PyH}^+]_{1h}}{[\text{PyH}^+]_0} \right). \quad (\text{Eq. 8})$$

$\alpha_0$  seems to increase with zeolite porosity (**Figure 5a**). **Figure 5b** shows that  $k_D$  and  $\alpha_1$  are also positively correlated, *i.e.* more active species will lead to a faster deactivation. This trend, however, seems to be somewhat mitigated on **JZO**, probably due to the secondary 16 MR porosity. While Brønsted acidity is intimately linked to initial activity and TOF (**Figure 3**), the ratio steady state activity/initial activity ( $\frac{\alpha_2}{\alpha_1 + \alpha_2} = \frac{\alpha_2}{\alpha_0}$ ) does not depend on the initial acidity (**Figure S4**), and remains in the range of 15 to 20% (only **FAU (6)** falls under 10%). Other factors considered as the degree of hierarchisation, BET surface area and acid sites density in the catalyst have no significant impact on this ratio (**Figure S4**). In addition, **Figure 5c** shows that  $\frac{\alpha_2}{\alpha_0}$  does not significantly depend on the availability of the acid sites, *i.e.* that some occupied acid sites still participate to the reaction, either by competitive adsorption of the reactants, or by activation of the adsorbed “deactivating” species. This behaviour was reported, for instance, in liquid and gas phase isomerisation and alkylation reactions of hydrocarbons [64].

**Figure 3** and **Figure 4** indicate the presence of an auto-inhibition effect of the Al sites proximity for **\*BEA** and **MOR**, as previously reported for **MFI** [48]. This inhibition is somewhat attenuated for **\*BEA** due to the interconnectivity (3D) of its channels, lacking on **MOR** (2D), where acid sites in the 8 MR side-pockets would play an additional role.

Zeolite structure and acidity do not therefore change the general deactivation pathways. For all catalysts, activity decreases to around 20% of its initial value before  $\alpha_1$  reaching steady state. The main

factor influencing activity is the catalyst total pore volume. The residual activity is not directly linked to the remaining accessible acid sites and thus “coke” participates to the anisole transformation. Initial TOF are highly dependent on acidity, with additional influences of both pore size (10, 12, 16 MR) and channel interconnectivity (2D – **MOR** – vs 3D – **FAU**, **\*BEA**, **JZO**). As a result, higher BAS concentrations tend to rapidly decrease initial activity and  $\text{TOF}_0$ , due to the auto-inhibition effect produced by higher adsorption energies induced by “paired” acid sites. This effect is enhanced by the low interconnectivity of the 2D zeolites (**MOR**) and mitigated with larger pore sizes in 3D, 12<sup>+</sup> MR zeolites (**\*BEA**, **FAU**, **JZO**). These larger pore openings and channels promote bimolecular reactions by largely mitigating (or eliminating) the steric hindrance of the channels.

## **2. 2. Products selectivities, structural and acidity effects.**

Anisole disproportionation on **MFI** zeolites mainly leads to transalkylation as the primary products (methylanisole and phenol), react further and methylated phenolates, such as cresols (secondary products), xylenols (tertiary products) and mesitols (further methylation of xylenols) appear in the product slate [20,22,48]. It is still the case for other zeolite structures, but some changes are noticeable, due either to acidity or structure.

**Figure 6** shows the evolution of conversion ( $X$ , wt.%) and main products selectivities ( $S_i$ , %) against time on stream for some of the catalysts (see **Figure S5** for all catalysts).

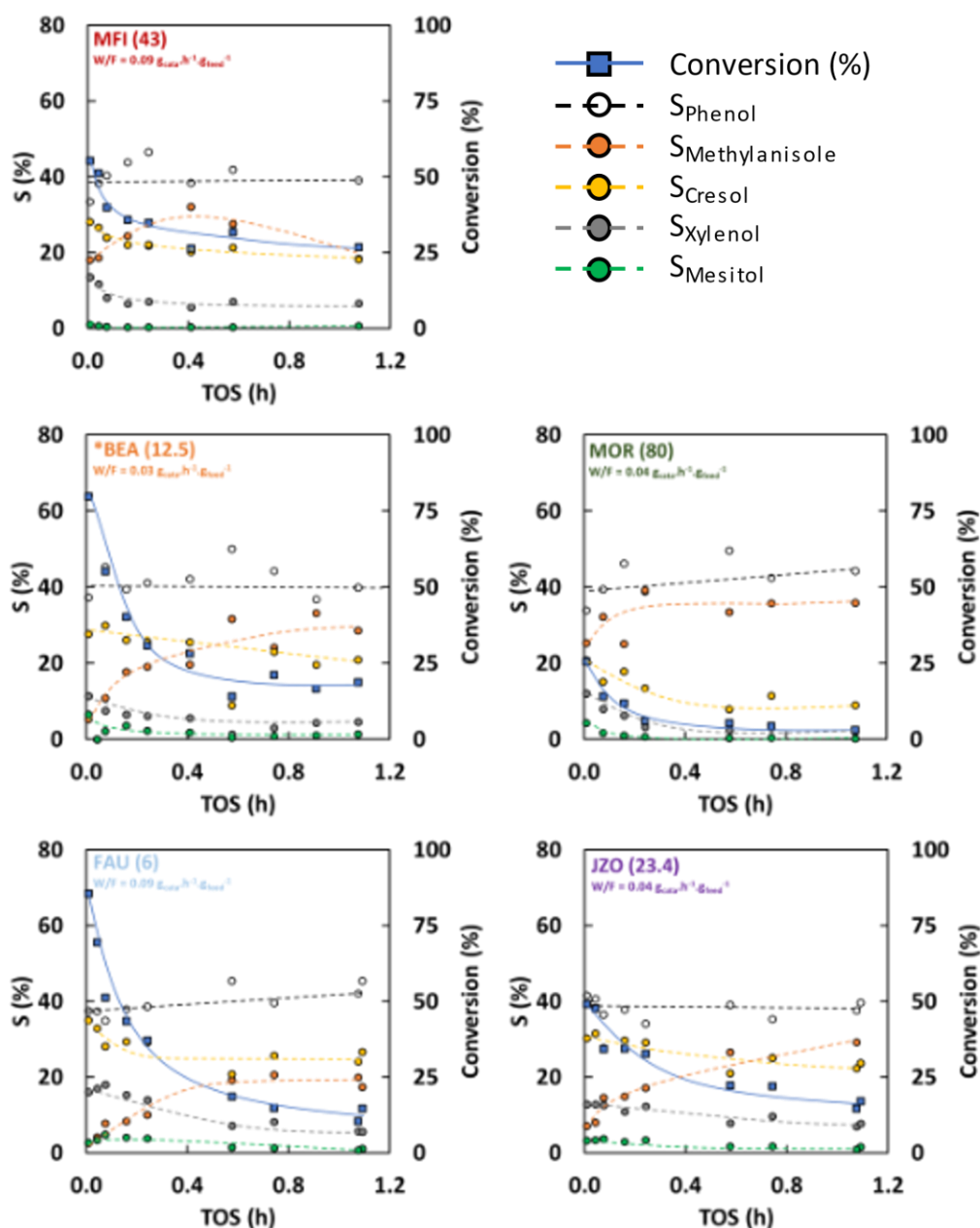
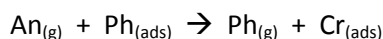


**Figure 6:** Anisole conversion and products selectivity for selected catalysts with time on stream.  $T = 673 \text{ K}$ ;  $P_{\text{An}} = 0.048 \text{ atm}$ ;  $P_{\text{tot}} = 1 \text{ atm}$ .

Phenol selectivity, around 40 wt.%, is mostly independently of the zeolite structure or acidity as most reactions involving anisole are producing phenol, compensating for its consumption in secondary reactions [22]. This confirms that the overall reaction pathway is not affected by catalyst structure and remains the same as previously reported for **MFI**.

Methylanisole selectivity follows the same pattern: it increases as conversion decreases and reaches a plateau at steady-state. The latter depends only on contact time, as was shown previously for **MFI** (43) [22]. Cresol selectivity evolves inversely to that of methylanisole, but again independently of structure and acidity. For most structures, when cresol and methylanisole selectivities cross before reaching their respective plateaus, the cause is the equilibrium between the two main paths to cresol production is shifted. It evolves from mainly **Reaction(1)** to mainly **Reaction(2)**:





**Reaction(2)**

Such an overtaking of **Reaction(1)** (hereafter called **Path I**) by **Reaction(2)** (hereafter called **Path II**) was visible in the coke composition on **MFI** from previous work, where more methylated products were present at higher TOS [22]. It is indicative of catalyst fouling by phenol adsorption followed by its methylation and these new active species participate to the steady-state conversion of anisole, and further methylation of the coke species. The continued presence of **Path I** even after its decrease as **Path II** dominates comes from the competitive adsorption of anisole and methylanisole on BAS, due to higher adsorption energies than  $(\text{Me})_x\text{Phenols}$  ( $-110$  to  $-145 \text{ kJ}\cdot\text{mol}^{-1}$  on single sites versus  $-82$  to  $-124 \text{ kJ}\cdot\text{mol}^{-1}$  for phenolics [22]).

Xylenol production follows the same pattern as cresol, leading to Mesityl production.

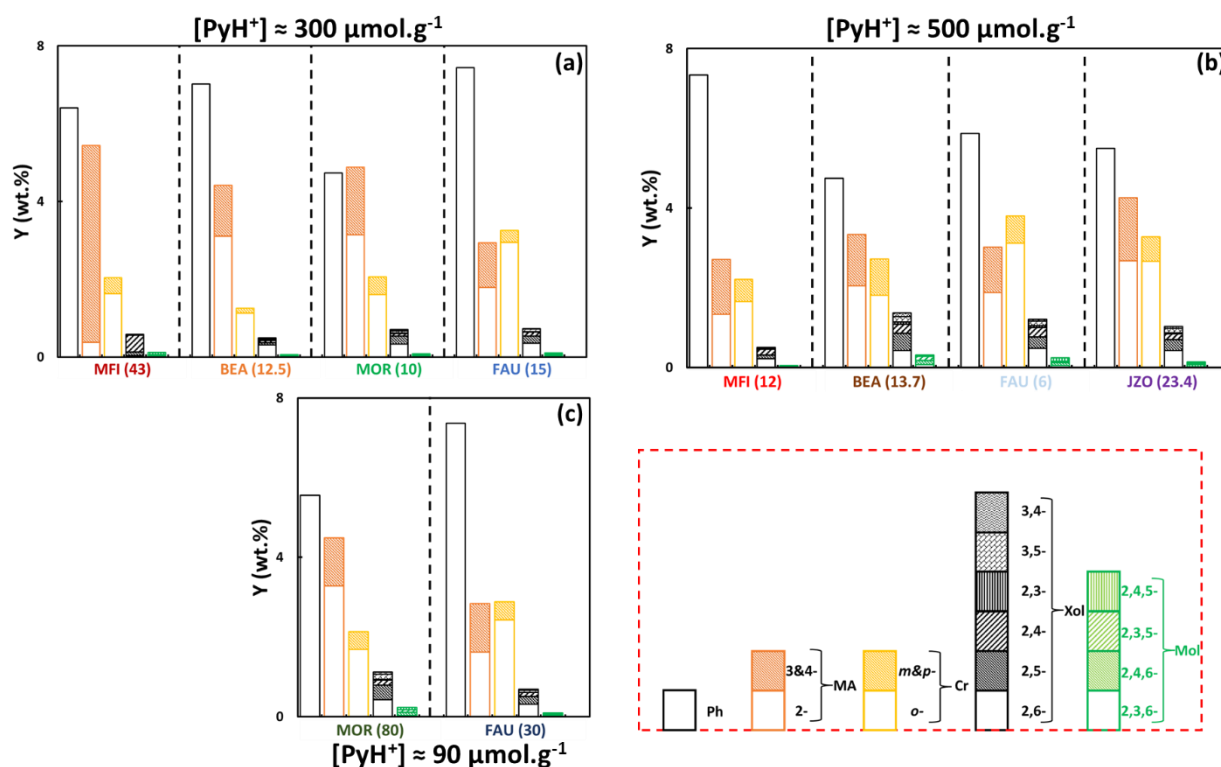


**Figure 7:** Isomers yields and distribution at identical conversion ( $X = 13.6 \pm 0.75 \%$ ) and acidity: catalysts at  $[\text{PyH}^+] \approx 300 \mu\text{mol}\cdot\text{g}^{-1}$ , **(b)**  $500 \mu\text{mol}\cdot\text{g}^{-1}$  and **(c)**  $90 \mu\text{mol}\cdot\text{g}^{-1}$ .

Ph: Phenol (White); MA: Methylanisole (Orange); Cr: Cresol (Yellow); Xol : Xylenol (Black); Mol : Mesityl (Green).

**Figure 7** displays the yields for the main products and their position isomers at isoconversion ( $\approx 13.6 \%$ ) for each catalysts, and at isoacidity (**Figure 7a**:  $300 \mu\text{mol}\cdot\text{g}^{-1}$ , **Figure 7b**:  $500 \mu\text{mol}\cdot\text{g}^{-1}$  and **Figure 7c**  $90 \mu\text{mol}\cdot\text{g}^{-1}$ ).

Previous work on **MFI** showed that the yields for the main products were not affected by acidity, but rather a function of conversion [48]. **MFI** (43) also showed a strong shape selectivity for the para of methylanisole, not found in the cresols (mainly the ortho- isomer). It was, however, found in the xylenol isomers in the coke: the combination of high shape selectivity towards p-MA, and high availability of the o-Cr increased the quantity of the 2,4-Xol in the product fraction as well as in the coke content (followed by a high proportion of 2,4,6-Mol when coke “aged”, after more reaction



time) [22]. The m-MA isomer is almost absent due to the o- and p- directing effect of the methoxy group, while the o-MA isomer is less produced, due to its steric hindrance.

In **MFI** (12), the higher shape selectivity for p-MA is absent due to the stronger retention of products on its BAS, in agreement with previous DFT calculations (with the increase of the concentration of acid sites, the para- and meta- isomers of MA are more strongly retained by the BAS, thus diffuse less easily out of the zeolite channels, and are therefore more likely to react with other molecules in the gas phase) [48]. This re-establishes the selectivity induced by the electronic effects for the ortho- and para- isomers. It also impacts the production of 2,4-Xol, no longer favoured compared to other Xol isomers.

For **FAU** and **\*BEA**, the higher acidity promotes transalkylations, and the production of Xol and Mol. It does not, however, promote significant changes in the isomer selectivity, with o-cresol staying the main Cr isomer. This is echoed by the higher selectivity for the 2,X- isomers of Xol (mainly X = 4, 5, 6 for steric reasons). **\*BEA** (13.7) and **FAU** (6) show much higher Xol and Mol yields than their less acidic counterparts. This is likely due to the faster fouling mentioned in **Figure 6** (and **Figure S5**) induced by their higher acidity and higher adsorption energies of the products.

As for the **MOR** catalysts, higher acidity produces the inverse effect of other structures: further methylation is no longer promoted by higher acidity, and it behaves as an **MFI**. **MOR** (10) is also the only catalyst with a higher MA than Ph selectivity. There is a slight decrease in Xol and Mol, but not in Cr. This implies an almost immediate fouling of the catalyst, similar to **MFI** (12), **\*BEA** (13.7) and **FAU** (6), and thus **Path II** is immediately favoured for the production of phenolics. This alone, however, does not entirely explain why MA is produced at a higher rate than Ph on **MOR** (10).

Mordenites possess 8 MR side pockets, accessible to molecules the size of toluene (here, Ph), where they can react [65]. MA, larger than Ph ( $\text{H}_3\text{C-O-} > \text{HO-}$ , plus methyl substituent), cannot access these side pockets and their BAS. This size-exclusion effect is not noticeable with **MOR** (80), most likely due to its weaker acidity and thus weaker adsorption of the products, which allows for already easier diffusion out of the channels.

Thus, zeolite structure has a clear effect on anisole disproportionation and isomer selectivity, but acidity also plays a role: the shape selectivity of **MFI** for p-MA is hindered by a higher BAS concentration, while the larger channels of **\*BEA**, **FAU** and **JZO** (and supercages of the latter two) promote bimolecular reactions and faster diffusion. Higher acidity in **FAU** shifts the Cr production equilibrium between **Paths I and II** towards the former. Finally, 2D zeolite **MOR** provides a unique product selectivity when paired with high acidity, due to the size exclusion effect of its side-pockets.

### 3. Coke formation and composition

The initial deactivation step of **MFI** during anisole disproportionation was attributed to the fast filling of the porous volume (and adsorption on the BAS) by the reaction products, so-called “oxygenated coke species”, and none of the habitual polyaromatic species were found in hydrocarbon transformation processes [22,48]. The next part provides information on the effect of zeolite structure on the composition of this unconventional “coke”.

**Figure 8** displays the distribution of the main coke components for each catalyst. These include the reaction products: phenol, cresol (methyl-phenol), xylenol (dimethyl-phenol), mesitol (trimethyl-phenol), as well as more methylated phenolics: durenol (tetramethyl-phenol) and pentamethyl-phenol. No anisole or methylanisole are detected. A notable addition is benzophenone, previously not identified due to background noise and impurities on the GC-MS chromatogram. Pentamethyl-phenol, previously unseen for similar reasons, is also found on each spent catalyst. Thus, structure and acidity do not significantly change the coke composition as it was reported previously on **MFI** (43) [22]. It was also suggested that there are two pathways of coke formation during transformation

and hydrodeoxygenation of bio-oil [63,64]. In addition to the polyaromatic coke which is formed by the usual mechanisms (hydrocarbon pool, condensation and growth of aromatic molecules) catalysed by the acid sites, there is also the formation of a more heterogeneous and oxygenated coke, formed by polymerization of some oxygenates derived from the pyrolysis of biomass components (lignin, cellulose and hemicellulose) at the external surface of the catalyst [66,67].

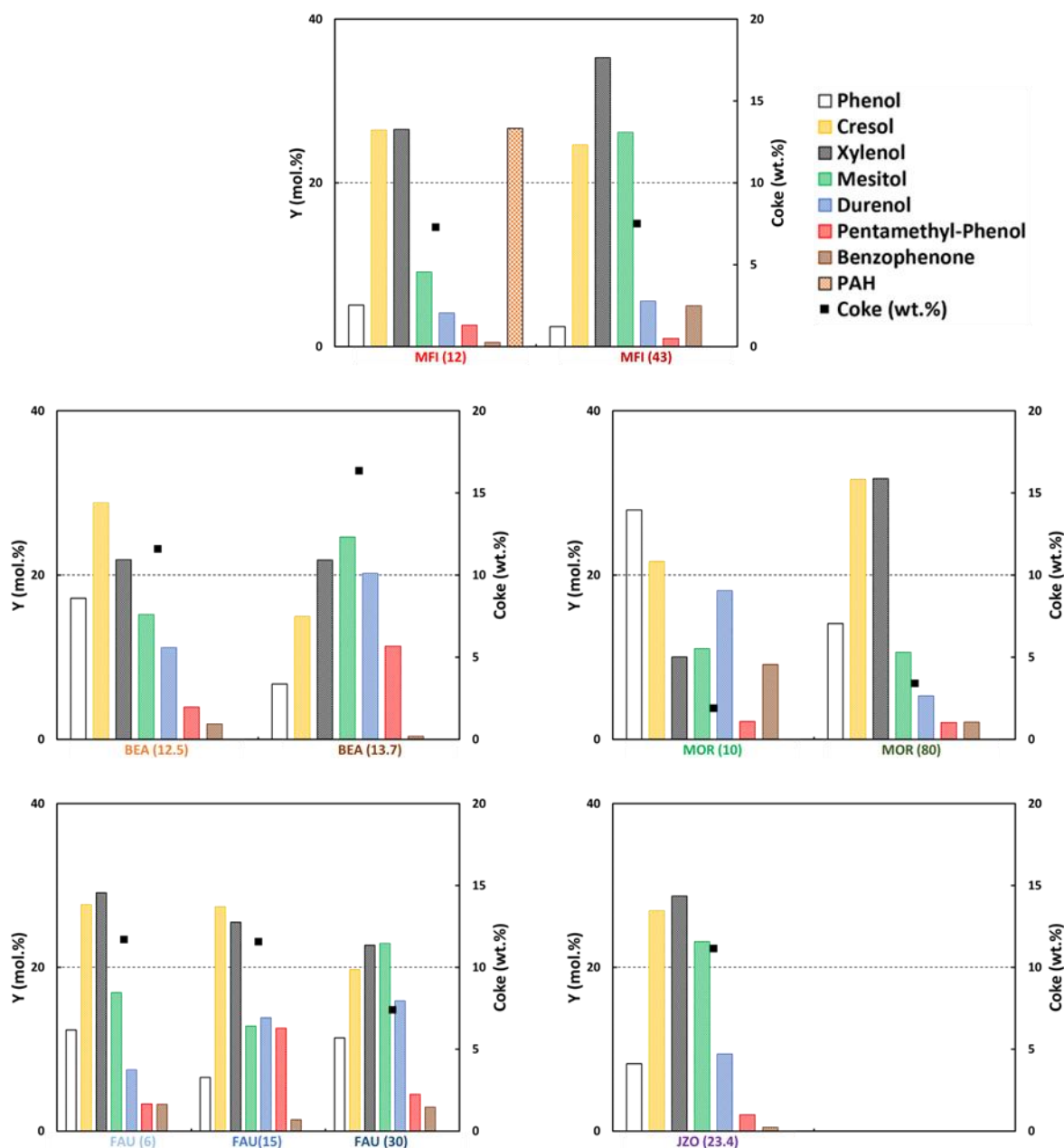


**Figure 8:** Quantification of the main coke components after 1h of reaction for each catalyst. (Y: fraction of the components in the soluble coke extract).

The quantification of the main species leads to the average molar mass and density presented in **Table 3**. These values are obtained via **Eq.9** and **Eq. 10** respectively:

$$\bar{M}_{coke} = \sum_i M_i x_{m_i} \quad (\text{Eq.9})$$

$$\bar{\rho}_{coke} = \sum_i \rho_i x_{m_i} \quad (\text{Eq.10})$$

With  $M_i$ ,  $\rho_i$  and  $x_{m_i}$  the molar mass, volumetric mass and mass fraction of each component of the coke mix. The components identified and used for the “PAH” group quantification are listed in **Table S1**.

While the coke quantity on the catalyst and its exact composition varies with zeolite structure and acidity, its average molar mass and density show fairly low variation: from 121 to 132  $\text{g}\cdot\text{mol}^{-1}$  and 0.99 to 1.03  $\text{g}\cdot\text{cm}^{-3}$  respectively.

**Table 3:** Average coke content, molar mass and density for each catalyst.

Structure	Si/Al	Coke (wt.%)	$\bar{M}_{coke}^a$ ( $\text{g}\cdot\text{mol}^{-1}$ )	$\bar{\rho}_{coke}$ ( $\text{g}\cdot\text{cm}^{-3}$ )
<b>MFI</b>	12	7.3	173.5	1.27
	43	7.6	123.1	1.02
<b>*BEA</b>	12.5	11.2	121.3	1.02
	13.7	14.9	132.3	1.00
<b>MOR</b>	10	1.9	124.3	1.03
	80	3.4	115.7	0.99
<b>FAU</b>	6	11.1	122.7	1.01
	15	10.3	128.3	1.00
	30	6.7	127.5	1.01
<b>JZO</b>	23.4	11.2	121.6	1.00

<sup>a</sup>: Estimated after identification of coke molecules by GC/MS and quantification by GC-FID.

The average coke contents are function of the available pore volume for each structure: the larger pores of the 3D **\*BEA**, **FAU** and **JZO** accommodate more coke (pore filling), while the 2D channels of **MOR** are easily obstructed, and thus allow for lower coke content (pore blocking, **Figure S6**) [68]. Higher anisole conversion also produces more coke.

As observed above for product shape selectivity, zeolite structure and acidity affect the distribution of the coke components: higher acidity in **\*BEA** shifts the composition towards more methylated products (mesitol, durenol, penta-methylphenol), while the weaker sites of **FAU** produce the inverse effect, primarily emphasizing the retention of cresol and xylenol [69].

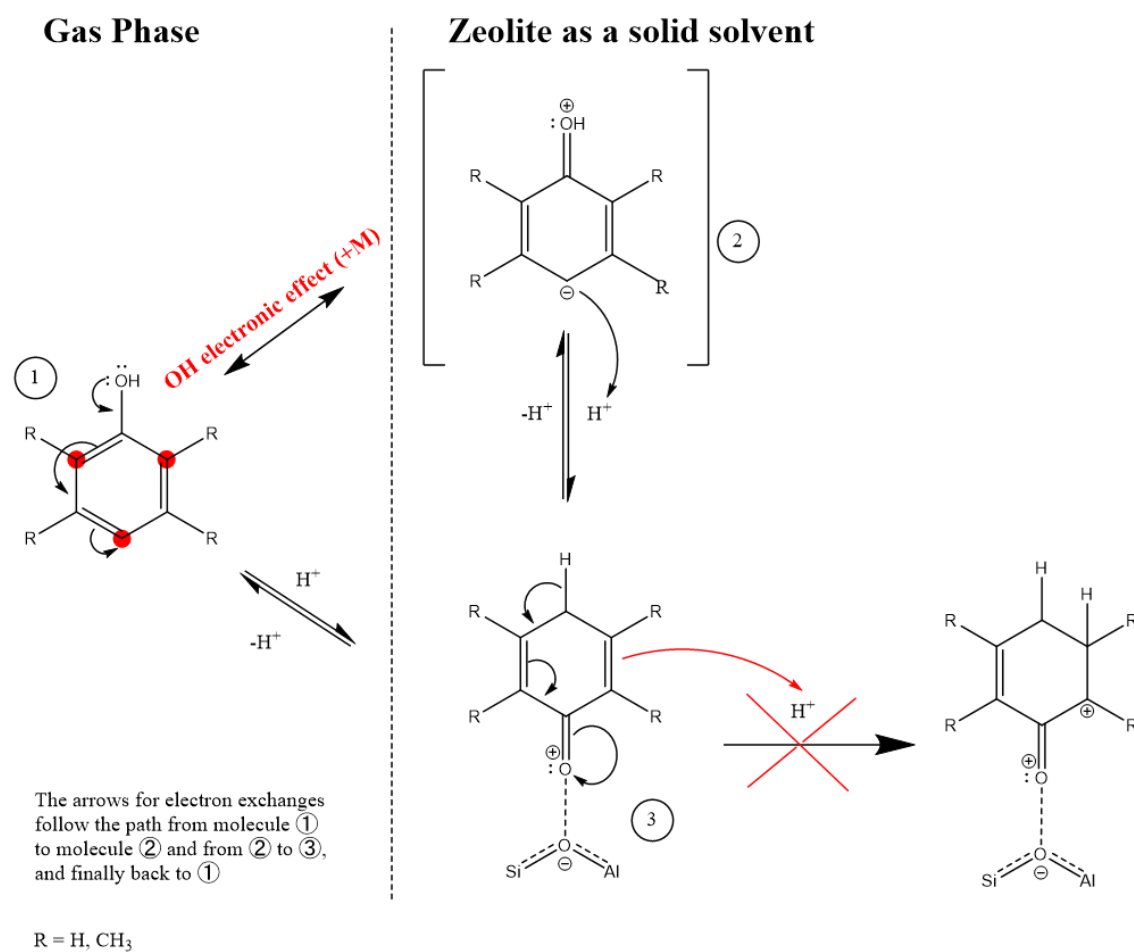
Notable exception, **MFI** (12) produces and retains conventional polyaromatic hydrocarbons (oxygenated and not, see **Table S1**), in addition to the retention of the reaction products. This implies that the combination of high acidity ( $641 \mu\text{mol}\cdot\text{g}^{-1}$ ) and smaller pore openings (10 MR) promotes the formation of polyaromatic coke, at low conversion, while it is inhibited on the other catalysts. The coke content between **MFI** (12) and **MFI** (43) does not vary significantly (7.3 wt.% and 7.6% respectively). However, since **MFI** (12) promotes the formation of PAH, the average coke molecular mass and density increase by  $50 \text{g}\cdot\text{mol}^{-1}$  and  $0.25 \text{g}\cdot\text{cm}^{-3}$  respectively.

Literature provides two conditions for coking through the Sullivan mechanism [39,40]. First, a steady source of alkylation on the aromatic cycles for the paring mechanism. In the present case, it occurs by multiple transalkylation reactions on the phenolics. Second, the ring contraction-expansion of the  $\text{C}_6$

aromatic cycle after carbon transfer via propylcarbenium cycle formation and opening should take place. The absence of alkyl groups bigger than methyl on the phenolics shows that this second condition is not fulfilled. Therefore, no polyaromatics are detected on the spent catalysts, except **MFI (12) (Figure 8)**, therefore the Sullivan mechanism (**Scheme S1**) does not occur. It was previously proposed that the hydroxyl function found in the extracted coke was responsible for inhibiting the ring contraction-expansion mechanism [22]. **Scheme 1** proposes an explanation for this inhibition:

The electronic effect of the hydroxyl group increases the electron density on the aromatic cycle (①), irrespective of its degree of methylation. The resulting mesomeric forms (②) all show a positive charge on the oxygen, and adsorption on the zeolite BAS stabilises this configuration (③), preventing the formation of carbenium species susceptible to induce the paring reaction in **Scheme S1** [39]. Similarly, this mesomeric effect and the resulting enhanced adsorption energies prevent bimolecular condensation reactions that would result in bulkier coke content [38].

The presence of some hydroxyl-substituted polyaromatic species on **MFI (12) (Figure 8)** shows that, either high acidity or the resulting high adsorption energies for the reaction products, help overcome the less-than favourable conditions for conventional coke formation. Chaouati et al. showed that, with low reactant partial pressure, another coke growth mechanism occurs by condensation (dehydrogenating coupling) of adsorbed species [38]. It is normally limited by high adsorption energies and higher reactant partial pressure.



**Scheme 1:** Proposed mechanism adsorption of (Me)<sub>x</sub> phenols on zeolite acid sites

In a nutshell, previous work on **MFI** showed that deactivation occurs by adsorption of reaction products on the active sites and fouling of the zeolite channels. It is extended here for other zeolitic materials. The nature of those deactivating species is not influenced by structure nor acidity, and only their distribution changes. The multiple methylations of the phenolic species could be likened to “aging” of the coke species. Those methyl-phenolics are present in the samples, even with the larger openings, in higher amount than their respective acid sites, thus they are most likely strongly adsorbed everywhere in the zeolite channels, and not only on Brønsted acid sites (fouling of the catalyst).

#### 4. Deactivation modes and “coke” toxicity

**Figure 9** shows the degradation of physico-chemical properties (Brønsted acidity and micropore volume) of the catalysts after 1h on stream. To avoid oxidation or desorption phenomena which may result from pre-treatment operations, precautions have been taken (degassing under vacuum at lower temperature and shorter time). **Figure 9a** compares the relative micropore volume loss measured by  $N_2$ -physisorption (**Eq. 11**) and the one calculated with  $\bar{\rho}_{coke}$  (**Eq. 12**).

$$V_{loss}^{N_2-phys} = \left(1 - \frac{V_{spent}}{V_0}\right)_{N_2-phys} \quad (\text{Eq. 11})$$

$$V_{loss}^{coke} = \left(\frac{\%coke}{100 \cdot \rho_{coke} \cdot V_0}\right) \quad (\text{Eq. 12})$$

These values are similar for most catalysts, indicating that  $N_2$  can access the whole porosity of the zeolites, even with the presence of high amounts of coke. Thus, there is no blockage (or plugging) of the channels by the “coke” species, as opposed to n-heptane cracking over **HFAU** (723 K, high coke content) [30]. This is explained by the relatively small size of these molecules, compared to the pore openings. They could diffuse in the channels without steric hindrance, especially for the larger pore openings if other factors were not involved [28].

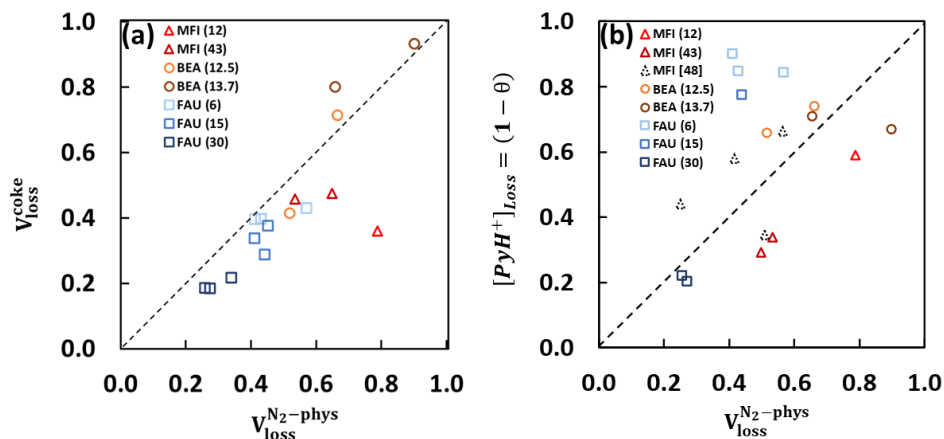


**Figure 9: (a)** Comparison between relative porous volume losses, measured by  $N_2$ -physisorption (**Eq. 9**) and calculated with the  $\bar{\rho}_{coke}$  at ToS = 1h (**Eq. 10**). **(b)** Measured relative acidity loss (**Eq. 11**) relative to apparent loss in microporous volume for **MFI**, **\*BEA** and **FAU** at ToS = 1h.

**Figure 9b** relates the relative acidity loss (**Eq. 13**) with the micropore volume loss (**Eq. 11**).

$$[PyH^+]_{Loss} = (1 - \theta) = \left(1 - \frac{[PyH^+]_{1h}}{[PyH^+]_0}\right) \quad (\text{Eq. 13})$$

Most of the data points are above or on the  $x = y$  dotted line, indicating that the acidity loss occurs at the same rate as the loss in micropore volume. Thus, there is no difference in accessibility between  $N_2$  and pyridine in the zeolite channels (for \***BEA**, **FAU** and **MFI**), and no partial or total pore blocking/plugging for the catalysts. The phenomenon of coke displacement by pyridine during Pyr-FTIR, previously mentioned for **MFI** [12,22], is responsible for an underestimation of the loss of acidity. It is observed for **MFI** as well as **FAU** and \***BEA** (**Figure S7**), thus explaining the position of the data points under the dotted line. There is no major loss of acidity without loss of porous volume, therefore an active site poisoning is unlikely.

Finally, **Figure 10** shows the relationship between the coke content and textural properties of the zeolites: **Figure 10a** plots the average number of coke molecules per available acid site against the initial acidity of the catalysts ( $[PyH^+]_0$ ). It shows that, with the exception of **MFI** (12) and **MOR** (10), every other zeolite holds multiple coke molecules per available acid site. While this number decreases with higher initial acidity, it shows that a majority of the coke molecules cannot adsorb onto BAS. It is therefore most likely adsorbed on silanols.

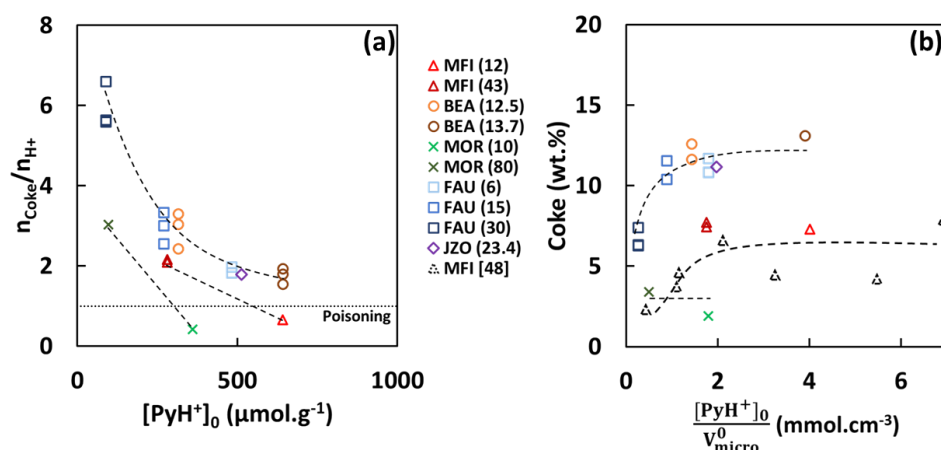


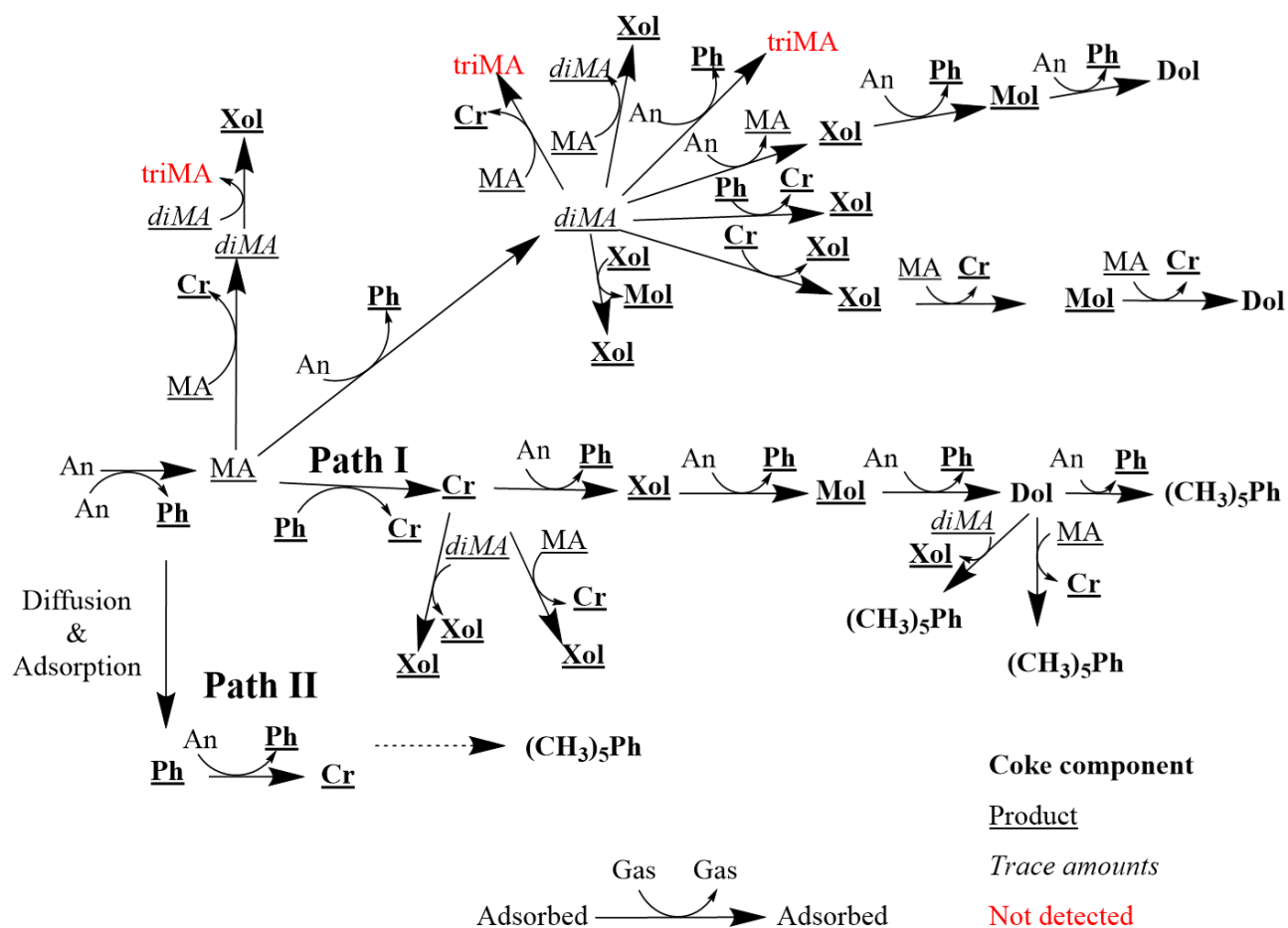
**Figure 10:** (a) Number of coke molecules per initial acid site relative to the catalyst acidity and (b) coke content relative to acid sites density in the microporous volume.

**Figure 10b** shows that coke content first increases with acid BAS density, to then level around 2  $\text{mmol.cm}^{-3}$  being then only function of the zeolite pore size and channel connectivity. The coke content therefore only depends on the surface available for adsorption, and, just as with **MFI**, the deactivation mode for anisole disproportionation is by fouling of the zeolite channels by adsorption of the phenolic compounds. Overall, although Phenol and its methyl derivatives are easily adsorbed and cover most of the zeolite, the coke toxicity to the acid sites is quite low, according to the steady-state observed for most catalysts.

**MFI** (12) holds less than 1 coke molecule per available acid site, while still holding the same coke weight as **MFI** (43). It is indicative of the growth of the conventional PAH species. As for **MOR** (10), the very low amount of coke in the spent catalyst explains the lower coke to BAS ratio.

Although phenol adsorption is strong on BAS, and is a deactivating factor in most cases, anisole disproportionation is an exception: the results in **Figures 4, 5** and **6**, with the low amount of phenol in the coke (**Figure 8**), lead to the conclusion that the steady-state is in part produced by the activation

of phenol, by its very adsorption, for the transalkylation reactions with anisole in the gas phase. Similarly, any anisole or methylanisole adsorbed on BAS are rapidly transformed into phenolics, thus explaining their absence from the coke make-up. Consequently, **Scheme 2** shows the proposed reaction “arborescence” for anisole disproportionation in acid zeolites. Whichever reaction path is followed, anisole stays the main reagent, and phenol the main product directly in the gas phase, as is the case no matter the conversion, contact time or catalyst.



**Scheme 2:** Proposed bimolecular reactions paths for anisole and its reaction products.

(An – Anisole; Ph – Phenol; MA – Methylanisole; Cr – Cresol; Xol – Xylenol; Mol – Mesityl; Dol – Durenol; diMA – Dimethylanisole; triMA – Trimethylanisole)

## Conclusion:

Zeolitic catalysts (10, 12 and 16 MR) with varying acidities, channel interconnectivity and crystal sizes were tested in anisole disproportionation, a model reaction to assess the behaviour of methoxy-aromatics during catalytic upgrading of primary pyrolysis products. Different zeolite structures produced the same light, oxygenated “coke” molecules (methyl-phenolics), independently of their pore sizes, channel geometry, etc. Acidity affects only the coke composition in **MFI**, probably in relation to the auto-inhibition effect of lower Si/Al ratios. These produced oxygenated derivatives of conventional PAH species (alcohols, methoxy, aldehyde, etc. substituted species). These are uncommon in literature, and their formation by the ring contraction-expansion mechanism is inhibited by the electronic effects of the oxygen groups. Here they are formed, probably via

condensation of the adsorbed species (another coke formation mechanism referenced to in literature, allowed by the low partial pressure of reactant).

## **Acknowledgements**

Nathan Pichot would like to thank the French Agence Nationale de la Recherche (ANR) and Région Nouvelle-Aquitaine for their financial support, through the PYCASSO and SHAPING projects. Similarly, Ludovic Pinard thanks the Région Normandie for their financial support, through the Bio/DNH project.

The authors thank the Xylofutur label for their support.

The authors acknowledge the precious work and help of Jean-Dominique Comparot (IC2MP), Valérie Riaux and Marie Lozier (LCS) for the Pyr-FTIR and N<sub>2</sub>-physisorption analyses

## **Declaration of competing interests**

The authors declare having no known competing financial or personal interests that could have influenced the work and results discussed in the present paper.

## **Authors contribution credit**

Nathan Pichot: Experimental work, data exploitation, first draft, review, editing.

Nourrdine Chaouati: Coke extraction, GC-MS analysis and exploitation, review, editing.

Thomas Lemaitre: Experimental work.

Mohamad Fahda: Catalyst synthesis and characterisation.

Svetlana Mintova, Valentin Valtchev: Review, editing.

Jean-Pierre Gilson: Discussion, review, editing.

Anthony Dufour: Supervision, funding, review, and editing.

Ludovic Pinard: Supervision, design of experimental work, data exploitation, funding, review, and editing.



## References

- [1] J.D. Adjaye, N.N. Bakhshi, Production of hydrocarbons by catalytic upgrading of a fast pyrolysis bio-oil. Part I: Conversion over various catalysts, (1995) 23.
- [2] T.R. Carlson, G.A. Tompsett, W.C. Conner, G.W. Huber, Aromatic Production from Catalytic Fast Pyrolysis of Biomass-Derived Feedstocks, *Top Catal* 52 (2009) 241–252. <https://doi.org/10.1007/s11244-008-9160-6>.
- [3] T.R. Carlson, Y.-T. Cheng, J. Jae, G.W. Huber, Production of green aromatics and olefins by catalytic fast pyrolysis of wood sawdust, *Energy Environ. Sci.* 4 (2011) 145–161. <https://doi.org/10.1039/C0EE00341G>.
- [4] T. Dickerson, J. Soria, Catalytic Fast Pyrolysis: A Review, *Energies* 6 (2013) 514–538. <https://doi.org/10.3390/en6010514>.
- [5] M. Hellinger, H.W.P. Carvalho, S. Baier, D. Wang, W. Kleist, J.-D. Grunwaldt, Catalytic hydrodeoxygenation of guaiacol over platinum supported on metal oxides and zeolites, *Applied Catalysis A: General* 490 (2015) 181–192. <https://doi.org/10.1016/j.apcata.2014.10.043>.
- [6] X. Xu, E. Jiang, Z. Li, Y. Sun, BTX from anisole by hydrodeoxygenation and transalkylation at ambient pressure with zeolite catalysts, *Fuel* 221 (2018) 440–446. <https://doi.org/10.1016/j.fuel.2018.01.033>.
- [7] H. Zhang, S. Shao, R. Xiao, D. Shen, J. Zeng, Characterization of Coke Deposition in the Catalytic Fast Pyrolysis of Biomass Derivates, *Energy Fuels* 28 (2014) 52–57. <https://doi.org/10.1021/ef401458y>.
- [8] S. Du, J.A. Valla, G.M. Bollas, Characteristics and origin of char and coke from fast and slow, catalytic and thermal pyrolysis of biomass and relevant model compounds, *Green Chem.* 15 (2013) 3214. <https://doi.org/10.1039/c3gc41581c>.
- [9] L.Y. Jia, M. Raad, S. Hamieh, J. Toufaily, T. Hamieh, M. Bettahar, G. Mauviel, M. Tarrighi, L. Pinard, A. Dufour, Catalytic fast pyrolysis of biomass : superior selectivity of hierarchical zeolite to aromatics, *Green Chem.* 19 (2017) 5442–5459. <https://doi.org/10.1039/C7GC02309J>.
- [10] I. Graça, J.-D. Comparot, S. Laforge, P. Magnoux, J.M. Lopes, M.F. Ribeiro, F.R. Ribeiro, Effect of phenol addition on the performances of H–Y zeolite during methylcyclohexane transformation, *Applied Catalysis A: General* 353 (2009) 123–129. <https://doi.org/10.1016/j.apcata.2008.10.032>.
- [11] I. Graça, A. Fernandes, J.M. Lopes, M.F. Ribeiro, S. Laforge, P. Magnoux, F. Ramôa Ribeiro, Effect of phenol adsorption on HY zeolite for n-heptane cracking: Comparison with methylcyclohexane, *Applied Catalysis A: General* 385 (2010) 178–189. <https://doi.org/10.1016/j.apcata.2010.07.011>.
- [12] I. Graça, J.-D. Comparot, S. Laforge, P. Magnoux, J.M. Lopes, M.F. Ribeiro, F. Ramôa Ribeiro, Influence of Phenol Addition on the H-ZSM-5 Zeolite Catalytic Properties during Methylcyclohexane Transformation, *Energy Fuels* 23 (2009) 4224–4230. <https://doi.org/10.1021/ef9003472>.
- [13] I. Graça, J.M. Lopes, M.F. Ribeiro, F. Ramôa Ribeiro, H.S. Cerqueira, M.B.B. de Almeida, Catalytic cracking in the presence of guaiacol, *Applied Catalysis B: Environmental* 101 (2011) 613–621. <https://doi.org/10.1016/j.apcatb.2010.11.002>.
- [14] I. Graça, F.R. Ribeiro, H.S. Cerqueira, Y.L. Lam, M.B.B. de Almeida, Catalytic cracking of mixtures of model bio-oil compounds and gasoil, *Applied Catalysis B: Environmental* 90 (2009) 556–563. <https://doi.org/10.1016/j.apcatb.2009.04.010>.
- [15] I. Graça, J.M. Lopes, M.F. Ribeiro, M. Badawi, S. Laforge, P. Magnoux, F. Ramôa Ribeiro, n-Heptane cracking over mixtures of HY and HZSM-5 zeolites: Influence of the presence of phenol, *Fuel* 94 (2012) 571–577. <https://doi.org/10.1016/j.fuel.2011.11.033>.
- [16] A.G. Gayubo, A.T. Aguayo, A. Atutxa, R. Aguado, J. Bilbao, Transformation of Oxygenate Components of Biomass Pyrolysis Oil on a HZSM-5 Zeolite. I. Alcohols and Phenols, *Ind. Eng. Chem. Res.* 43 (2004) 2610–2618. <https://doi.org/10.1021/ie030791o>.

- [17] A.G. Gayubo, A.T. Aguayo, A. Atutxa, B. Valle, J. Bilbao, Undesired components in the transformation of biomass pyrolysis oil into hydrocarbons on an HZSM-5 zeolite catalyst, *J. Chem. Technol. Biotechnol.* 80 (2005) 1244–1251. <https://doi.org/10.1002/jctb.1316>.
- [18] J.D. Adjaye, N.N. Bakhshi, CATALYTIC CONVERSION OF A BIOMASS-DERIVED OIL TO FUELS AND CHEMICALS I: MODEL COMPOUND STUDIES AND REACTION PATHWAYS, (n.d.).
- [19] S. Du, D.P. Gamliel, M.V. Giotto, J.A. Valla, G.M. Bollas, Coke formation of model compounds relevant to pyrolysis bio-oil over ZSM-5, *Applied Catalysis A: General* 513 (2016) 67–81. <https://doi.org/10.1016/j.apcata.2015.12.022>.
- [20] X. Zhu, R.G. Mallinson, D.E. Resasco, Role of transalkylation reactions in the conversion of anisole over HZSM-5, *Applied Catalysis A: General* 379 (2010) 172–181. <https://doi.org/10.1016/j.apcata.2010.03.018>.
- [21] T. Prasomsri, A.T. To, S. Crossley, W.E. Alvarez, D.E. Resasco, Catalytic conversion of anisole over HY and HZSM-5 zeolites in the presence of different hydrocarbon mixtures, *Applied Catalysis B: Environmental* (2011) S0926337311002347. <https://doi.org/10.1016/j.apcatb.2011.05.026>.
- [22] N. Pichot, J.W. Hounfodji, M. Badawi, V. Valtchev, S. Mintova, J.-P. Gilson, A. Dufour, L. Pinard, Products and coke shape-selectivity during anisole disproportionation over HZSM-5, *Applied Catalysis A: General* 665 (2023) 119352. <https://doi.org/10.1016/j.apcata.2023.119352>.
- [23] T. Zhang, C. Bhattarai, Y. Son, V. Samburova, A. Khlystov, S.A. Varganov, Reaction Mechanisms of Anisole Pyrolysis at Different Temperatures: Experimental and Theoretical Studies, *Energy Fuels* 35 (2021) 9994–10008. <https://doi.org/10.1021/acs.energyfuels.1c00858>.
- [24] Y.-T. Cheng, G.W. Huber, Chemistry of Furan Conversion into Aromatics and Olefins over HZSM-5: A Model Biomass Conversion Reaction, *ACS Catal.* 1 (2011) 611–628. <https://doi.org/10.1021/cs200103j>.
- [25] J.-L. Grandmaison, P.D. Chantal, S.C. Kaliaguine, Conversion of furanic compounds over H-ZSM-5 zeolite, *Fuel* 69 (1990) 1058–1061. [https://doi.org/10.1016/0016-2361\(90\)90020-Q](https://doi.org/10.1016/0016-2361(90)90020-Q).
- [26] P.D. Chantal, S. Kaliaguine, J.L. Grandmaison, Reactions of phenolic compounds over HZSM-5, *Applied Catalysis* 18 (1985) 133–145. [https://doi.org/10.1016/S0166-9834\(00\)80304-8](https://doi.org/10.1016/S0166-9834(00)80304-8).
- [27] Q. Meng, H. Fan, H. Liu, H. Zhou, Z. He, Z. Jiang, T. Wu, B. Han, Efficient Transformation of Anisole into Methylated Phenols over High-Silica HY Zeolites under Mild Conditions, *ChemCatChem* 7 (2015) 2831–2835. <https://doi.org/10.1002/cctc.201500479>.
- [28] M. Guisnet, P. Magnoux, Coking and deactivation of zeolites: Influence of the Pore Structure, *Applied Catalysis* 54 (1989) 1–27. [https://doi.org/10.1016/S0166-9834\(00\)82350-7](https://doi.org/10.1016/S0166-9834(00)82350-7).
- [29] P. Magnoux, P. Roger, C. Canaff, V. Fouche, N.S. Gnep, M. Guisnet, New Technique for the Characterization of Carbonaceous Compounds Responsible for Zeolite Deactivation, in: *Studies in Surface Science and Catalysis*, Elsevier, 1987: pp. 317–330. [https://doi.org/10.1016/S0167-2991\(09\)60370-0](https://doi.org/10.1016/S0167-2991(09)60370-0).
- [30] M. Guisnet, L. Costa, F.R. Ribeiro, Prevention of zeolite deactivation by coking, *Journal of Molecular Catalysis A: Chemical* 305 (2009) 69–83. <https://doi.org/10.1016/j.molcata.2008.11.012>.
- [31] M. Argyle, C. Bartholomew, Heterogeneous Catalyst Deactivation and Regeneration: A Review, *Catalysts* 5 (2015) 145–269. <https://doi.org/10.3390/catal5010145>.
- [32] A. Bonnin, Y. Pouilloux, V. Coupard, D. Uzio, L. Pinard, Deactivation mechanism and regeneration study of Zn/HZSM-5 catalyst in ethylene transformation, *Applied Catalysis A: General* 611 (2021) 117976. <https://doi.org/10.1016/j.apcata.2020.117976>.
- [33] J. Oudar, *Deactivation and Poisoning of Catalysts*, Taylor & Francis, 1985. <https://books.google.fr/books?id=FSa1zLeJL1sC>.
- [34] S. Laforge, D. Martin, M. Guisnet, m-Xylene transformation over H-MCM-22 zeolite. 2. Method for determining the catalytic role of the three different pore systems, *Microporous and Mesoporous Materials* 67 (2004) 235–244. <https://doi.org/10.1016/j.micromeso.2003.11.008>.
- [35] M. Guisnet, P. Magnoux, Organic chemistry of coke formation, *Applied Catalysis A: General* 212 (2001) 83–96. [https://doi.org/10.1016/S0926-860X\(00\)00845-0](https://doi.org/10.1016/S0926-860X(00)00845-0).

- [36] M. Guisnet, F.R. Ribeiro, eds., Deactivation and regeneration of zeolite catalysts, Imperial College Press ; Distributed by World Scientific, London : Singapore, 2011.
- [37] R. Setton, ed., Chemical Reactions in Organic and Inorganic Constrained Systems, Springer Netherlands, Dordrecht, 1986. <https://doi.org/10.1007/978-94-009-4582-1>.
- [38] N. Chaouati, A. Soualah, M. Chater, M. Tarighi, L. Pinard, Mechanisms of coke growth on mordenite zeolite, *Journal of Catalysis* 344 (2016) 354–364. <https://doi.org/10.1016/j.jcat.2016.10.011>.
- [39] R.F. Sullivan, C.J. Egan, G.E. Langlois, R.P. Sieg, A New Reaction That Occurs in the Hydrocracking of Certain Aromatic Hydrocarbons, *J. Am. Chem. Soc.* 83 (1961) 1156–1160. <https://doi.org/10.1021/ja01466a036>.
- [40] R. Sullivan, Hydrocracking of alkylbenzenes and polycyclic aromatic hydrocarbons on acidic catalysts. Evidence for cyclization of the side chains, *Journal of Catalysis* 3 (1964) 183–195. [https://doi.org/10.1016/0021-9517\(64\)90126-5](https://doi.org/10.1016/0021-9517(64)90126-5).
- [41] L. Pinard, S. Hamieh, C. Canaff, F. Ferreira Madeira, I. Batonneau-Gener, S. Maury, O. Delpoux, K. Ben Tayeb, Y. Pouilloux, H. Vezin, Growth mechanism of coke on HBEA zeolite during ethanol transformation, *Journal of Catalysis* 299 (2013) 284–297. <https://doi.org/10.1016/j.jcat.2012.12.018>.
- [42] S. Lee, M. Choi, Unveiling coke formation mechanism in MFI zeolites during methanol-to-hydrocarbons conversion, *Journal of Catalysis* 375 (2019) 183–192. <https://doi.org/10.1016/j.jcat.2019.05.030>.
- [43] J. Valecillos, H. Vicente, A.G. Gayubo, A.T. Aguayo, P. Castaño, Spectro-kinetics of the methanol to hydrocarbons reaction combining online product analysis with UV–vis and FTIR spectroscopies throughout the space time evolution, *Journal of Catalysis* 408 (2022) 115–127. <https://doi.org/10.1016/j.jcat.2022.02.021>.
- [44] M. Luo, D. Wang, B. Hu, Y. Fu, G. Mao, B. Wang, The Molecular Structure and Morphology of Insoluble Coke in SAPO-34 Catalyst, *ChemistrySelect* 2 (2017) 5458–5462. <https://doi.org/10.1002/slct.201700930>.
- [45] Z. Ma, E. Troussard, J.A. van Bokhoven, Controlling the selectivity to chemicals from lignin via catalytic fast pyrolysis, *Applied Catalysis A: General* 423–424 (2012) 130–136. <https://doi.org/10.1016/j.apcata.2012.02.027>.
- [46] P. Sirous Rezaei, H. Shafaghat, W.M.A.W. Daud, Suppression of coke formation and enhancement of aromatic hydrocarbon production in catalytic fast pyrolysis of cellulose over different zeolites: effects of pore structure and acidity, *RSC Adv.* 5 (2015) 65408–65414. <https://doi.org/10.1039/C5RA11332F>.
- [47] Z. Liu, X. Dong, X. Liu, Y. Han, Oxygen-containing coke species in zeolite-catalyzed conversion of methanol to hydrocarbons, *Catal. Sci. Technol.* 6 (2016) 8157–8165. <https://doi.org/10.1039/C6CY01463A>.
- [48] N. Pichot, J.W. Hounfodji, H. El Siblani, M. Badawi, V. Valtchev, S. Mintova, J.-P. Gilson, A. Dufour, L. Pinard, Anisole disproportionation on HZSM-5: the key role of Si/Al ratio on auto-inhibition effect, *Applied Catalysis A: General* (2024) 119565. <https://doi.org/10.1016/j.apcata.2024.119565>.
- [49] Q.-F. Lin, Z.R. Gao, C. Lin, S. Zhang, J. Chen, Z. Li, X. Liu, W. Fan, J. Li, X. Chen, M.A. Cambor, F.-J. Chen, A stable aluminosilicate zeolite with intersecting three-dimensional extra-large pores, *Science* 374 (2021) 1605–1608. <https://doi.org/10.1126/science.abk3258>.
- [50] M. Fahda, J. Fayek, E. Dib, H. Cruchade, N. Chaouati, L. Pinard, P. Petkov, A. Mayoral, B. Witulski, L. Lakiss, V. Valtchev, Optimizing the synthesis and probing the acidic properties of an extra-large pore aluminosilicate, Submitted for publication (2024).
- [51] J. Ward, The nature of active sites on zeolites IX. Sodium hydrogen zeolite, *Journal of Catalysis* 13 (1969) 364–372. [https://doi.org/10.1016/0021-9517\(69\)90445-X](https://doi.org/10.1016/0021-9517(69)90445-X).
- [52] C. Miranda, J. Urresta, H. Cruchade, A. Tran, M. Benghalem, A. Astafan, P. Gaudin, T.J. Daou, A. Ramírez, Y. Pouilloux, A. Sachse, L. Pinard, Exploring the impact of zeolite porous voids in liquid

- phase reactions: The case of glycerol etherification by tert-butyl alcohol, *Journal of Catalysis* 365 (2018) 249–260. <https://doi.org/10.1016/j.jcat.2018.07.009>.
- [53] A. Beuque, M. Barreau, E. Berrier, J.-F. Paul, N. Batalha, A. Sachse, L. Pinard, Transformation of Dilute Ethylene at High Temperature on Micro- and Nano-Sized H-ZSM-5 Zeolites, (2021).
- [54] MFI: Framework Type, (n.d.). <https://europe.iza-structure.org/IZA-SC/framework.php?STC=MFI> (accessed February 6, 2024).
- [55] Beta: DO Family, (n.d.). [https://europe.iza-structure.org/IZA-SC/DO\\_structures/DO\\_material\\_rm.php?IFN=Beta](https://europe.iza-structure.org/IZA-SC/DO_structures/DO_material_rm.php?IFN=Beta) (accessed February 6, 2024).
- [56] MOR: Framework Type, (n.d.). <https://europe.iza-structure.org/IZA-SC/framework.php?STC=MOR> (accessed February 6, 2024).
- [57] FAU: Framework Type, (n.d.). <https://europe.iza-structure.org/IZA-SC/framework.php?STC=FAU> (accessed February 6, 2024).
- [58] JZO: Framework Type, (n.d.). <https://europe.iza-structure.org/IZA-SC/framework.php?STC=JZO> (accessed February 6, 2024).
- [59] K.S.W. Sing, Reporting physisorption data for gas/solid systems with special reference to the determination of surface area and porosity (Recommendations 1984), *Pure and Applied Chemistry* 57 (1985) 603–619. <https://doi.org/10.1351/pac198557040603>.
- [60] K.S.W. Sing, R.T. Williams, Physisorption Hysteresis Loops and the Characterization of Nanoporous Materials, *Adsorption Science & Technology* 22 (2004) 773–782. <https://doi.org/10.1260/0263617053499032>.
- [61] S. Bordiga, C. Lamberti, F. Bonino, A. Travert, F. Thibault-Starzyk, Probing zeolites by vibrational spectroscopies, *Chemical Society Reviews* 44 (2015) 7262–7341. <https://doi.org/10.1039/C5CS00396B>.
- [62] A. Bonnin, J.-D. Comparot, Y. Pouilloux, V. Coupard, D. Uzio, L. Pinard, Mechanisms of aromatization of dilute ethylene on HZSM-5 and on Zn/HZSM-5 catalysts, *Applied Catalysis A: General* 611 (2021) 117974. <https://doi.org/10.1016/j.apcata.2020.117974>.
- [63] M. Huang, S. Kaliaguine, A. Auroux, Lewis basic and Lewis acidic sites in zeolites, in: *Studies in Surface Science and Catalysis*, Elsevier, 1995: pp. 311–318. [https://doi.org/10.1016/S0167-2991\(06\)81903-8](https://doi.org/10.1016/S0167-2991(06)81903-8).
- [64] M. Guisnet, “Coke” molecules trapped in the micropores of zeolites as active species in hydrocarbon transformations, *Journal of Molecular Catalysis A: Chemical* 182–183 (2002) 367–382. [https://doi.org/10.1016/S1381-1169\(01\)00511-8](https://doi.org/10.1016/S1381-1169(01)00511-8).
- [65] H. Issa, J. Toufaily, T. Hamieh, J.D. Comparot, A. Sachse, L. Pinard, Mordenite etching in pyridine: Textural and chemical properties rationalized by toluene disproportionation and n-hexane cracking, *Journal of Catalysis* 374 (2019) 409–421. <https://doi.org/10.1016/j.jcat.2019.05.004>.
- [66] B. Valle, P. Castaño, M. Olazar, J. Bilbao, A.G. Gayubo, Deactivating species in the transformation of crude bio-oil with methanol into hydrocarbons on a HZSM-5 catalyst, *Journal of Catalysis* 285 (2012) 304–314. <https://doi.org/10.1016/j.jcat.2011.10.004>.
- [67] T. Cordero-Lanzac, R. Palos, I. Hita, J.M. Arandes, J. Rodríguez-Mirasol, T. Cordero, J. Bilbao, P. Castaño, Revealing the pathways of catalyst deactivation by coke during the hydrodeoxygenation of raw bio-oil, *Applied Catalysis B: Environmental* 239 (2018) 513–524. <https://doi.org/10.1016/j.apcatb.2018.07.073>.
- [68] G. Froment, Deactivation of zeolite catalysts by coke formation, *Journal of Catalysis* 124 (1990) 391–400. [https://doi.org/10.1016/0021-9517\(90\)90187-O](https://doi.org/10.1016/0021-9517(90)90187-O).
- [69] L. Rollmann, Shape selectivity and carbon formation in zeolites, *Journal of Catalysis* 56 (1979) 139–140. [https://doi.org/10.1016/0021-9517\(79\)90099-X](https://doi.org/10.1016/0021-9517(79)90099-X).